

## Supporting Information

### Protonation/ Reduction Dynamics at the [4Fe-4S] Subsite of the Hydrogen-forming Cofactor of [FeFe]-Hydrogenases

Moritz Senger<sup>†</sup>, Stefan Mebs<sup>‡</sup>, Jifu Duan<sup>#</sup>, Olga Shulenina<sup>⊥</sup>, Konstantin Laun<sup>†</sup>, Leonie Kertess<sup>#</sup>, Florian Wittkamp<sup>§</sup>, Ulf-Peter Apfel<sup>§</sup>, Thomas Happe<sup>#</sup>, Martin Winkler<sup>#</sup>, Michael Haumann<sup>‡</sup>, Sven T. Stripp<sup>†</sup>

<sup>†</sup> Department of Physics, Experimental Molecular Biophysics, Freie Universität Berlin, 14195 Berlin, Germany

<sup>‡</sup> Department of Physics, Biophysics of Metalloenzymes, Freie Universität Berlin, 14195 Berlin, Germany

<sup>#</sup> Faculty of Biology and Biotechnology, Photobiotechnology, Ruhr-Universität Bochum, 44801 Bochum, Germany

<sup>⊥</sup> Faculty of Physics, St. Petersburg State University, 198504 St. Petersburg, Russian Federation

<sup>§</sup> Faculty of Chemistry and Biochemistry, Inorganic Chemistry I, Ruhr-Universität Bochum, 44801 Bochum, Germany

## Contents

Table S1	<b>Vibrational frequencies for Hox and HoxH</b>
Figure S1	<b>Reduction of methyl viologen via dithionite in the aerosol</b>
Figure S2	<b>Global fit analysis and experimental uncertainty</b>
Figure S3	<b>Verification of the aerosol-mediated pH titration</b>
Figure S4	<b>Influence of DT on Hox → HoxH conversion</b>
Figure S5	<b>Further kinetic studies</b>
Figure S6	<b>Influence of protein concentration, hydration level, and temperature</b>
Figure S7	<b>Formation of HoxH-CO and HoxH</b>
Figure S8	<b>Sulfur/ Selenium exchange</b>
Figure S9	<b>H/D exchange, KIE, and cofactor integrity</b>
Figure S10	<b>Population of reduced states in HYDA1<sup>adt</sup> in presence of H<sub>2</sub></b>
Figure S11	<b>Inter-molecular electron transfer in hydrogenase films</b>
Figure S12	<b>Model structures for DFT</b>
Figure S13	<b>Calculation results for model and theory level variation</b>
Figure S14	<b>DFT on Hox and HoxH</b>
Figure S15	<b>DFT on Hox-CO and HoxH-CO</b>
Figure S16	<b>DFT on Hred´ and Hred´H</b>
Figure S17	<b>Vibrational modes, spin densities, and charges from DFT</b>
Figure S18	<b>Putative proton path to the [4Fe-4S] cluster in CPI</b>
Figure S19	<b>Accumulation of HoxH and basic reaction cycle</b>
Figure S20	<b>Numerical simulations of HoxH formation</b>

**Table S1A – Vibrational Frequencies of Hox and HoxH.** Native CPI, DDH, and HYDA1 as well as amino acid variante C169D and C169A of HYDA1.

(A)	enzyme	variation	vCN		vCO		
			<i>p</i>	<i>d</i>	<i>p</i>	<i>d</i>	$\mu$
Hox	CPI	native	2081	2069	1970	1947	1801
	DDH	native	2090	2078	1965	1940	1802
	HYDA1	native	2088	2017	1964	1940	1802
		C169D	2087	2071	1964	1940	1803
		C169A	2087	2068	1962	1938	1804
HoxH	CPI	native	2085	2074	1975	1953	1808
	DDH	native	2098	2083	1972	1947	1812
	HYDA1	native	2092	2075	1970	1946	1812
		C169D	2093	2075	1971	1947	1812
		C169A	2092	2075	1972	1946	1813

**Table S1B – Vibrational Frequencies of Hox and HoxH.** HYDA1 cofactor variants odt, sdt, pdt, and edt. Legend: p - proximal, d - distal,  $\mu$  - bridging. See Fig. 3 for spectra.

(B)	enzyme	variation	vCN		vCO		
			<i>p</i>	<i>d</i>	<i>p</i>	<i>d</i>	$\mu$
Hox	HYDA1	odt	2088	2070	1963	1942	1804
		sdt	2087	2069	1970	1943	1803
		pdtd	2090	2073	1966	1941	1810
		edt	2088	2073	1965	1940	1808
HoxH	HYDA1	odt	2094	2078	1974	1950	1813
		sdt	2093	2076	1973	1950	1814
		pdtd	2092	2075	1970	1945	1812
		edt	2094	2076	1969	1945	1814

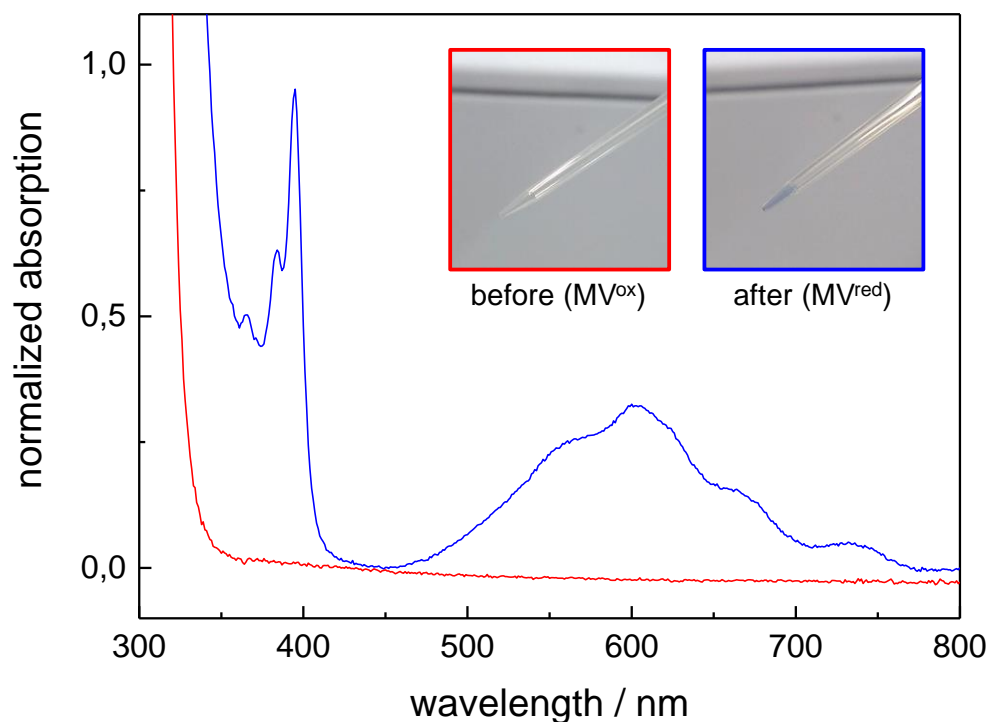


**Fig. S1 – Reduction of methyl viologen via dithionite in the aerosol.** 2  $\mu\text{L}$  oxidized methyl viologen (MV, 500 mM in oxygen-free water (Millipore), see photo with the red frame) was used to form a film on the ATR crystal. The red trace shows the UV/vis spectrum recorded prior to film formation (Ocean Optics mini-spectrometer USB2000 equipped with an IMPLEN Sub-Micro Liter Cell). Methyl viologen was dried and rehydrated under  $\text{N}_2$  aerosol enriched with 200 mM sodium dithionite (DT) solution. The aerosol treatment was continued with  $1.5 \text{ L min}^{-1}$  for 30 minutes. Afterwards, the film was removed from the ATR crystal with 2  $\mu\text{L}$  oxygen-free water. Visual inspection suggested reduction of MV (photo with the blue frame) and the spectrum identified the absorption bands of MV (most prominent at 395 nm and 605 nm) and DT (310 nm). This proof-of-concept experiment shows how soluble components like DT “fly” with the aerosol and can be deposited in the film on the ATR crystal, e.g. MV or protein.

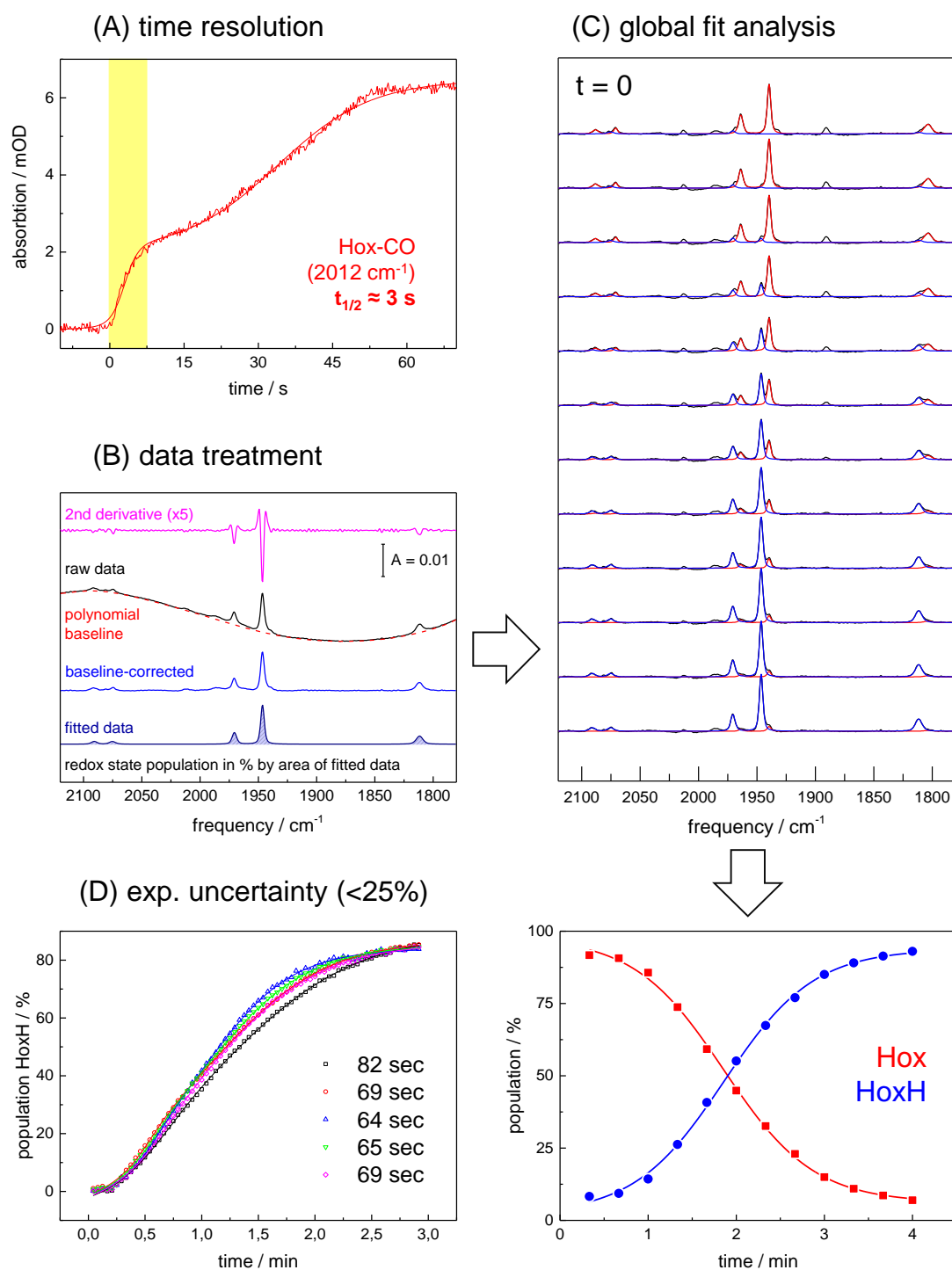


**Fig. S2 – Time resolution, global fit analysis, and experimental uncertainty.** (A) CO binding to a film of oxidized HYDA1 followed by ATR FTIR. The increase of the marker band at  $2012 \text{ cm}^{-1}$  is followed over time (80 kHz, single scan forward/ backward, spectral resolution  $8 \text{ cm}^{-1}$ ). Accumulation of **Hox-CO** shows a biphasic behavior with  $t_{1/2} \sim 3$  s (yellow area) and  $\sim 35$  s. Making use of flash-photolysis QCL IR spectroscopy, Mirmohades et al. measured  $t_{1/2}$

~15 ms for CO binding to **Hox**. Clearly, CO inhibition cannot be followed by conventional FTIR spectroscopy. The value of ~3 s thus represents the timescale of equilibration in the aerosol set-up (the latter process might be associated with diffusion of gas through the thick protein film and similar “bulk” phenomena). Data acquisition (~200 ms for 80 kHz scanning velocity, 8 cm<sup>-1</sup> spectral resolution, and individual analysis of spectra) is not limiting to this process. **(B)** Second derivative spectra (magenta) were used to identify band positions. Fitting of raw spectra (black) using a polynomial defined the baseline (red). Baseline-corrected spectra (blue) were fitted with sets of Voigt functions (50% Gaussian/ 50% Lorentzian character, dark blue) to obtain band amplitudes, widths, and relative intensities of individual H-cluster species as input parameters for the global fit analysis of spectra from H-cluster state mixtures. The summed area of observed bands (2 CN<sup>-</sup>, 3 CO) is referred to as “population” and given in % throughout the text (the oscillator strengths are approximately the same in all analyzed redox states). Data processing and curve fitting was performed with inhouse software. **(C)** Baseline-corrected spectra for a typical **Hox** to **HoxH** conversion (from top to bottom and red to blue colours). Band widths and relative intensities for each H-cluster species were kept constant in the fit. Lower panel: H-cluster state populations plotted over reaction time. **(D)** Estimation of experimental uncertainty from repeated population of **HoxH** from **Hox** for five individual protein films. The relative error in the determination of the half-time (or rate) of **HoxH** formation was estimated as <25 %.

Reference:

Mirmohades, M. et al. Following [FeFe] Hydrogenase Active Site Intermediates by Time-Resolved Mid-IR Spectroscopy. *J. Phys. Chem. Lett.* 7, 3290–3293 (2016).

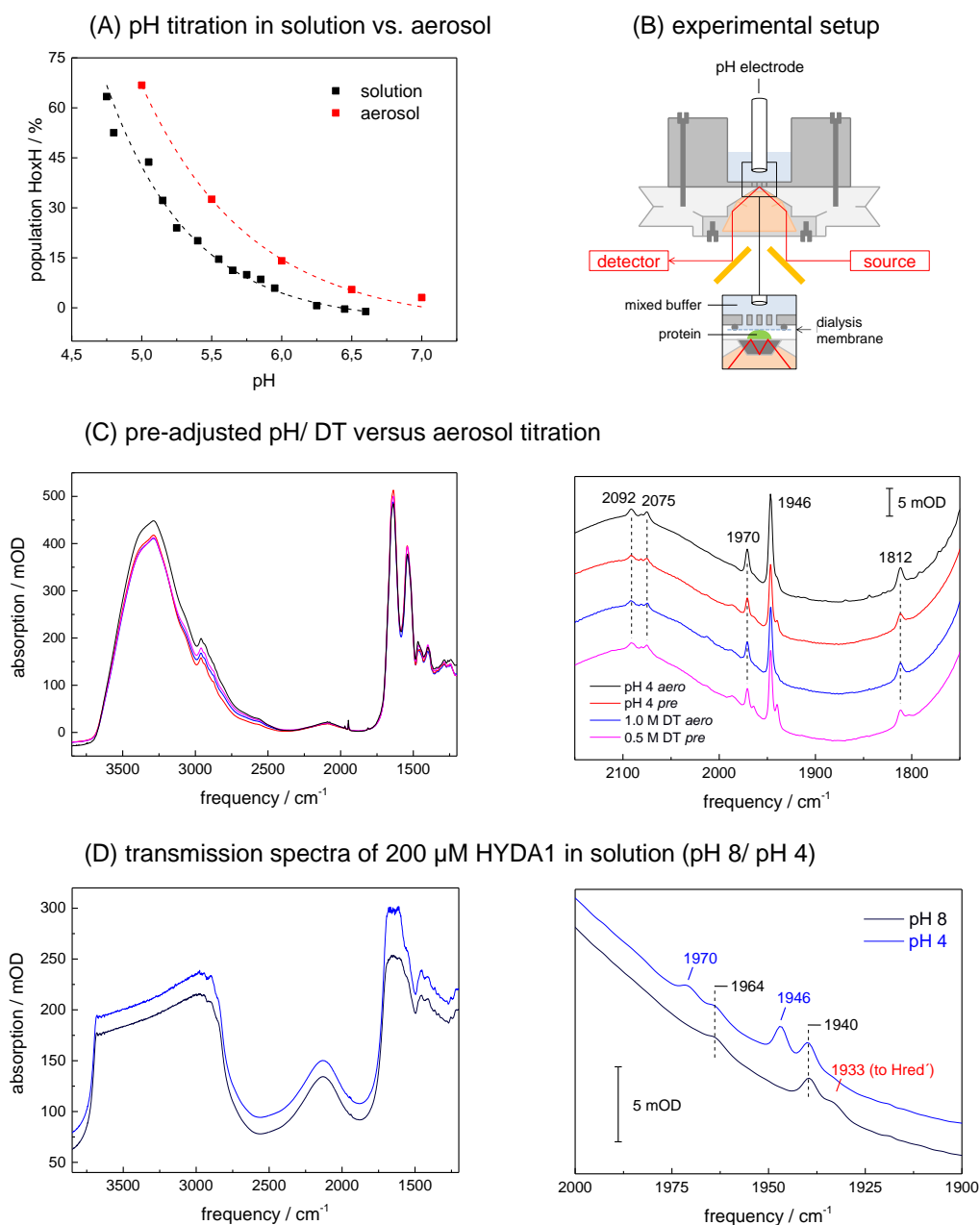


**Fig. S3 – Verification of the aerosol-mediated pH titration.** (A) Population yield of **HoxH** as a function of pH in solution (black) and via aerosol (red). The pH difference was estimated as  $\sim 0.25$  units in the aerosol vs. solution experiments. (B) For the solution-based titration, a pH electrode was used to directly measure the pH in the medium covering the enzyme (the buffer penetrated a semi-permeable 8 kDa dialysis membrane to protect the protein film from dilution). (C) Standard HYDA1 preparations as titrated to pH 4 (black) or 1 M DT (blue) via the aerosol (aero) are compared to protein as isolated at pH 4 (red) or pre-adjusted to 0.5 M DT (magenta). The respective spectra predominantly show **HoxH** in all cases. (D) Transmission spectra of 200  $\mu\text{M}$  HYDA1 at pH 8 and pH 4 (left panel; 2 mM DT each,  $\text{CaF}_2$  sandwich samples with 50  $\mu\text{m}$  spacer). Right panel: pCO/ dCO spectrum. At pH 4, a mixture of **Hox** and **HoxH** is observed (blue trace) whereas at pH 8 (black trace) **Hox** dominates.

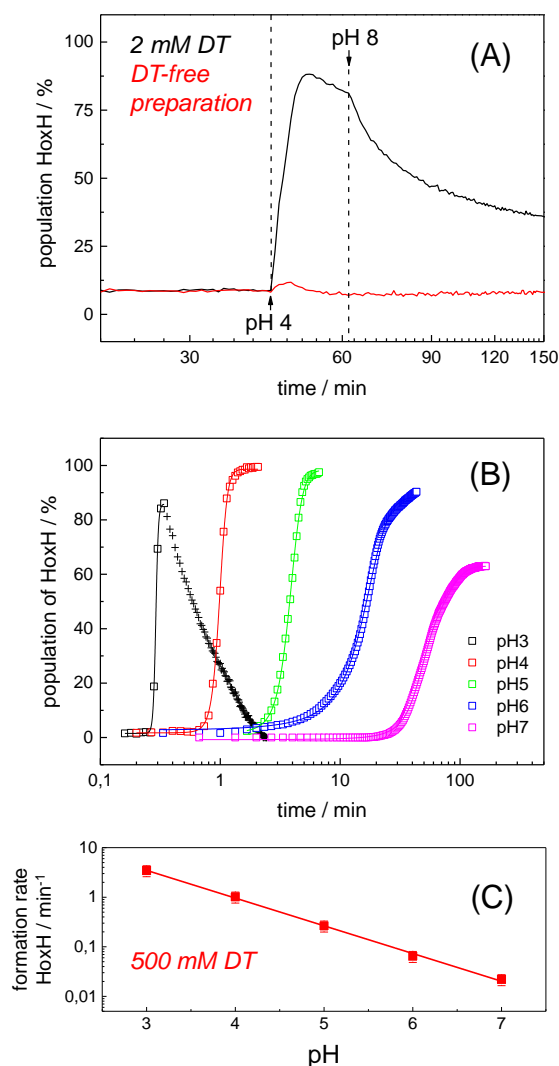


**Fig. S4 - Influence of DT on Hox → HoxH conversion. (A)** In presence of 2 mM DT (black trace), a change from pH 8 to pH 4 induced a steep increase of **HoxH** in HYDA1<sup>adt</sup>. The process is reversible; conversion back to **Hox** was achieved when the buffer pH was changed back to pH 8. HYDA1 as isolated in the absence of DT (red trace) did not show significant **HoxH** population in response to sample acidification (the small IR change around  $t = 0$  is due to a minor transient change in sample hydration due to the aerosol change). **(B)** Time course of HYDA1<sup>adt</sup> **HoxH** formation at 500 mM DT for changing the pH from 8 to the indicated values (pH 3 – pH 7). Note the decrease of the IR signal at pH 3 that follows the population of **HoxH** (crosses, black trace), reflecting cofactor disintegration, which was absent during the experimental time period for pH values of 4 or larger. **(C)** Corresponding **HoxH** formation rates plotted vs. pH. Note the linear relation of the rate constant on a logarithmic scale to the pH (logarithmic proton concentration) over a range of four pH units.

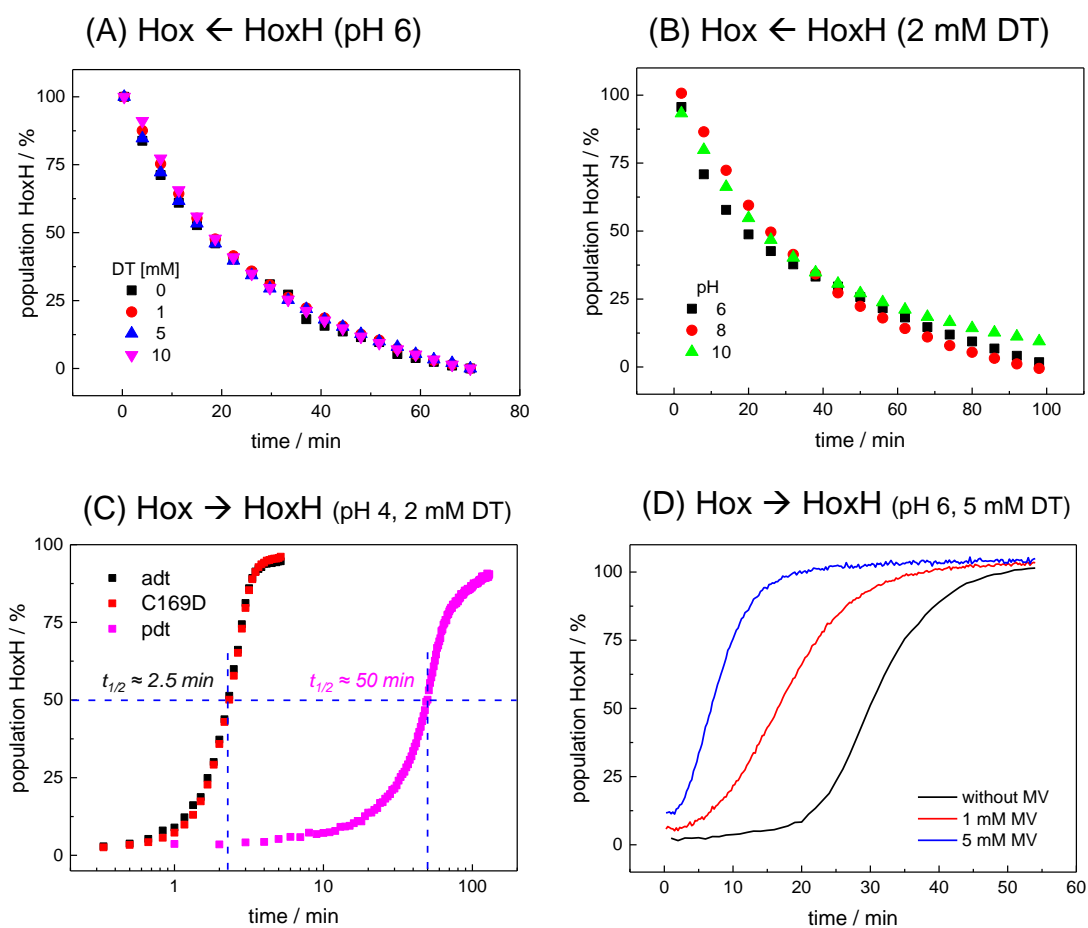


**Fig. S5 - Further kinetic studies.** Time course of back-conversion of **HoxH**  $\rightarrow$  **Hox** for (A) changing the DT concentration from 100 mM to the indicated values at pH 6 or for (B) changing the pH from 4 to the indicated values at 2 mM DT. (C) Time course of **HoxH** formation at pH 4 and 2 mM DT in HYDA1<sup>adt</sup> wild-type (black) and C169D (red) as well as cofactor variant HYDA1<sup>pdt</sup> (magenta). About 20-fold slower **HoxH** formation was observed in the pdt variant (see blue lines for estimation of  $t_{1/2}$ ). (D) Accelerated **HoxH** formation at 5 mM DT and pH 6 for increasing the concentration of the redox mediator methyl viologen (MV) from 0 to 5 mM (data correspond to relative intensities of the dCO band of **HoxH**).

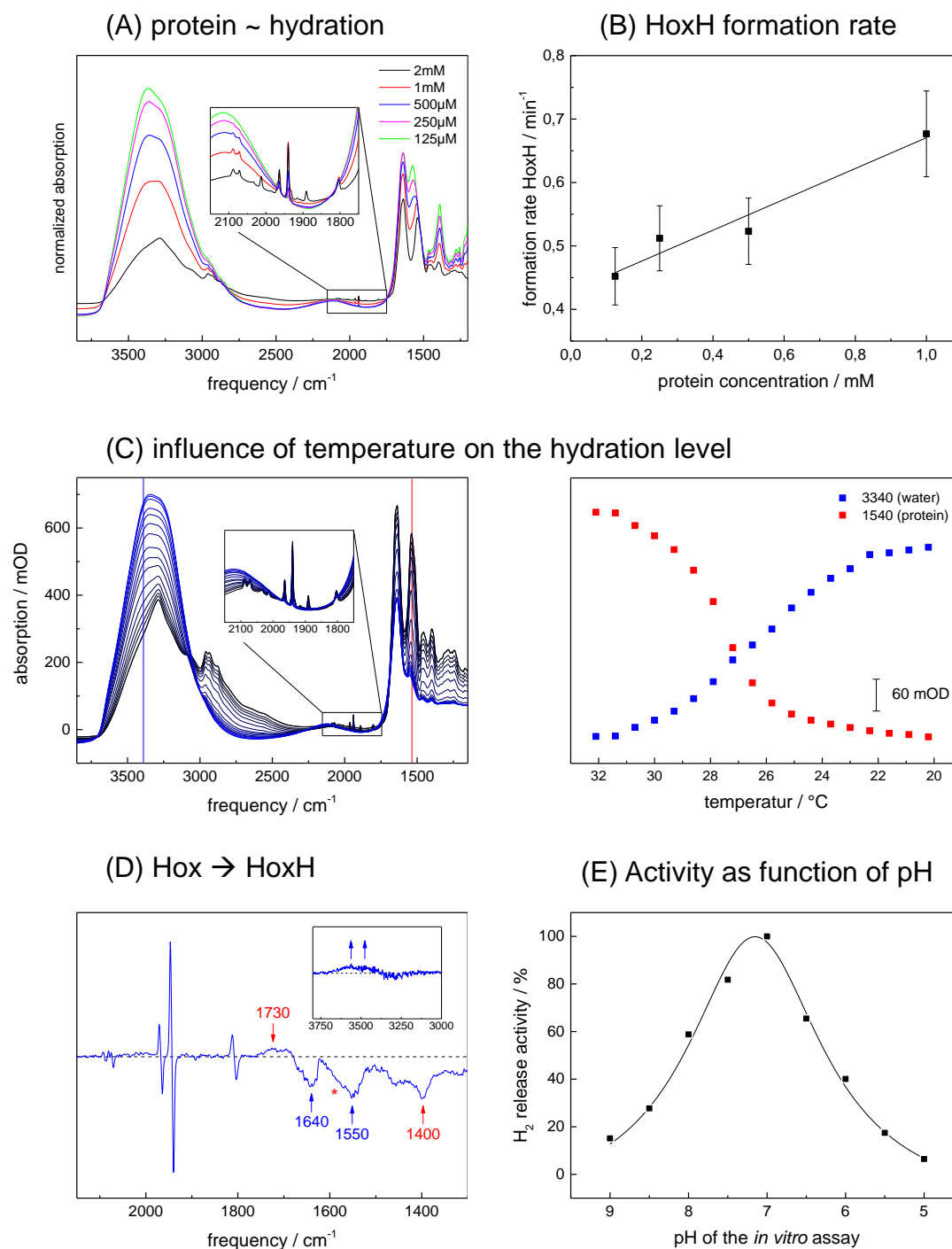
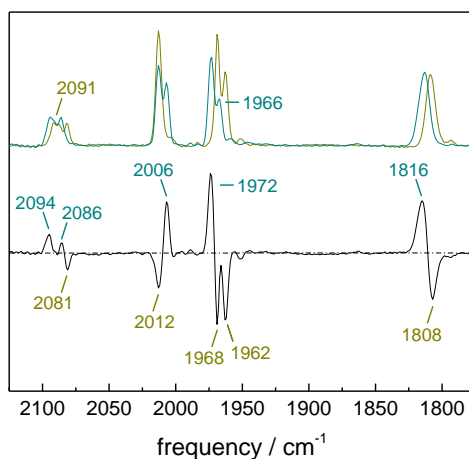


**Fig. S6 – Influence of protein concentration, hydration level, and temperature.** (A) HYDA1 was diluted with buffer from 2 – 0.125 mM protein prior to formation of protein films. For decreasing protein concentrations (P), normalized spectra (amide II, 1540  $\text{cm}^{-1}$ ) show an increase in hydration level (W, e.g. 3390  $\text{cm}^{-1}$ ). Protein signals are overlaid by buffer absorption but the decrease of cofactor bands (inset) immediately hints at decreasing protein levels.

**(B)** The **HoxH** formation rate was found to be affected by the P/W ratio. The influence is rather small. **(C)** Variation of crystal plate temperature ( $T_{cp}$ ) via a custom-made thermostat from 32 – 20°C strongly affected the P/W ratio. For  $T_{cp} > RT$  dehydration of sample was observed while  $T_{cp} < RT$  promoted an increase of water in the film. **(D)** With all parameters under control (esp. temperature and mass flow), titration could be performed without significant variation in P/W. A standard titration with 1.5 L min<sup>-1</sup> at 24°C from pH 8 to pH 4 (2 mM DT) is shown (same dataset as in **Fig. 3AB**). The **HoxH**-minus-**Hox** difference spectrum comprises a minor decrease in amide I (~1640 cm<sup>-1</sup>) and amide II (~1550 cm<sup>-1</sup>) band intensities due to film swelling. Accordingly, small difference bands in the asymmetric/ symmetric OH stretching frequencies of liquid water were detected (inset, asymmetric: 3390 cm<sup>-1</sup>, symmetric: 3280 cm<sup>-1</sup>). The stable P/W ratio facilitated identification of negative bands at 1400 cm<sup>-1</sup> and ~1590 cm<sup>-1</sup> (asterisks) both which can be assigned to carboxylate vibrations. Around 1730 cm<sup>-1</sup>, a positive feature indicates an increase of carboxylic acid groups. Together, the IR difference spectrum clearly suggests an acidification of the film. No indications for structural changes (i.e. distinct amide I difference bands) of the hydrogenase protein within a pH range of 4 - 8 were observed. **(E)** *In vitro* H<sub>2</sub> release activity as a function of pH. 100 ng native HYDA1 was diluted in 2 mL mixed buffer (50 mM) including 200 mM DT and no MV. The test tube was purged with argon and incubated at 37°C for 30 minutes. Afterwards, 1 mL of the gas phase was analyzed for H<sub>2</sub> by gas chromatography. The H<sub>2</sub> release activity is given relative to the maximal value at pH 7 (100%). For both pH > 7 and pH < 7 a steep decrease of activity was observed.

(A) Hox-CO & HoxH-CO



(B) Population of HoxH-CO

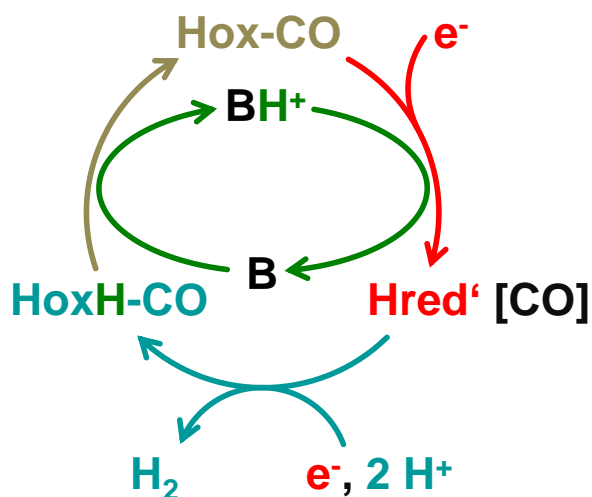


**Fig. S7 – Formation of HoxH-CO.** (A) The IR spectrum of HYDA1<sup>adt</sup> in the CO-inhibited state (**Hox-CO**) at pH 8 (dark-yellow) is compared to the IR spectrum that was obtained at ~60 min after changing the pH to 4 in the presence of 1% CO and 2 mM DT in the aerosol (dark-cyan). The latter state is denoted **HoxH-CO**. The black line shows the pH 4 – 8 difference spectrum. (B) Modified reaction cycle that explains the formation of **HoxH-CO** as a function of pH and DT. Reduction of **Hox-CO** weakens the iron-carbonyl bond of the externally added CO ligand (so that the CO is transiently detached). Oxidation of **Hred<sup>+</sup>** via H<sub>2</sub> release restores an oxidized species (i.e., **HoxH**), which is re-converted into a CO-inhibited species (**HoxH-CO**) in the presence of CO gas.

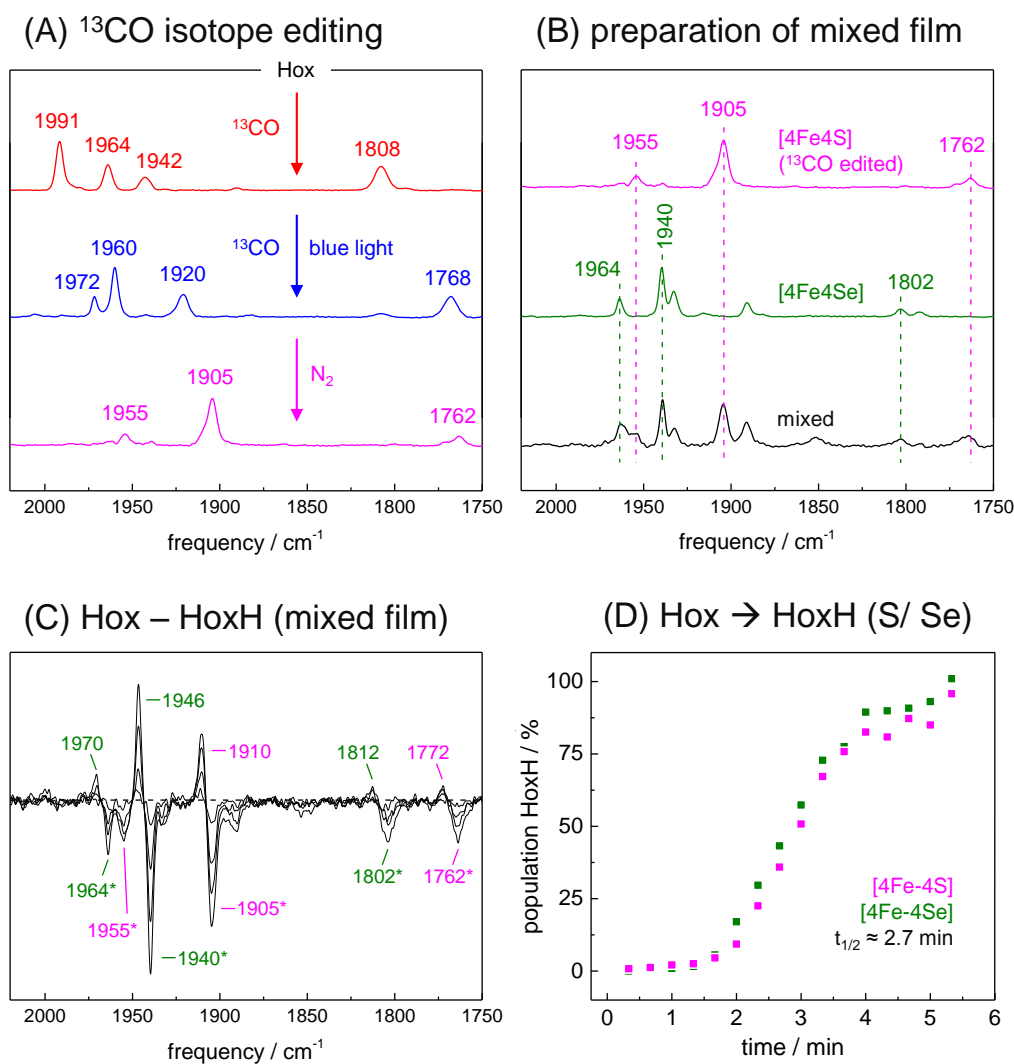


**Fig. S8 – Sulfur/ Selenium exchange.** (A)  $^{13}\text{CO}$  isotope editing of **Hox-CO** in wild-type  $\text{HYDA1}^{\text{adt}}$  (dCO and  $\mu\text{CO}$ ) due to exposure to  $^{13}\text{CO}$  gas (red), blue light irradiation (blue), and recovery of **Hox** under  $\text{N}_2$  (magenta). The CO region is shown. Protocol after Senger et al., PNAS 2016. (B) Co-deposition of  $^{13}\text{CO}$ -edited  $\text{HYDA1}^{\text{adt}}$  (magenta) and a  $\text{HYDA1}^{\text{adt}}$  with a [4Fe-4Se] cluster (green) and no  $^{13}\text{CO}$  ligands. The film shows a 50:50 mixture of **Hox** bands from both samples (black). Dashed lines mark respective **Hox** band positions. Co-deposition was chosen to facilitate pH titration under identical conditions for unambiguous band assignment and kinetics determination. (C) IR difference spectra collected on the mixed film during a change from pH 8 to 4 in the presence of 2 mM DT. Indicated frequencies are assigned to the respective **Hox** (negative bands) or **HoxH** species (positive bands) in the two variants (magenta/ green as above). (D) Time course of the **HoxH** yield for [4Fe-4S] and [4Fe-4Se] variants as determined from acidification of the mixed protein film. Both variants show a similar half-time of **HoxH** formation of  $\sim 2.7$  min, meaning that an effect of Se substitution on **HoxH** yield or formation rate was not discernible.

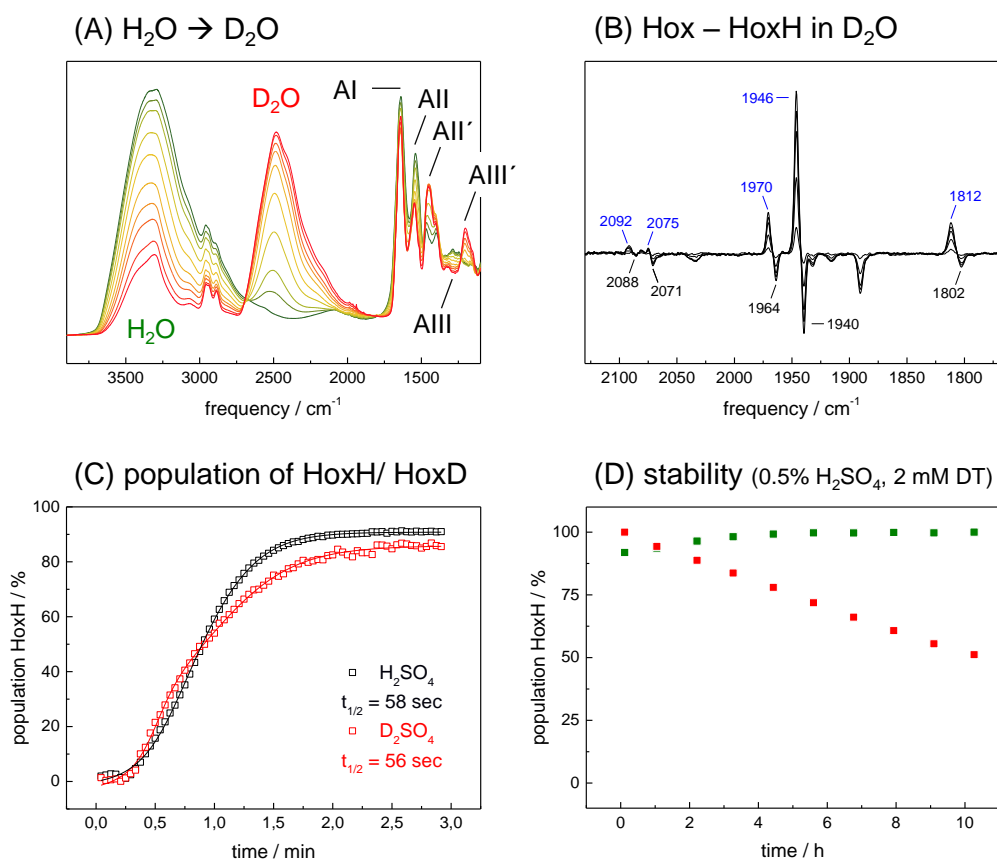


**Fig. S9 - H/D exchange, KIE, and cofactor integrity.** (A) Quantitative H<sub>2</sub>O → D<sub>2</sub>O exchange in the protein film on the ATR cell occurred when the aerosol was enriched with D<sub>2</sub>O by passing the gas stream through a respective buffer as monitored by the decrease of the H<sub>2</sub>O band around ~3400 cm<sup>-1</sup> and concomitant increase of the D<sub>2</sub>O band at ~2500 cm<sup>-1</sup>. AI – AIII: amide I – III vibrations of the protein backbone (AII' and AIII' denote the respective vibrations in D<sub>2</sub>O buffer). (B) HYDA1<sup>act</sup> was matured and isolated in D<sub>2</sub>O buffer. Infrared spectra were collected with D<sub>2</sub>O in the aerosol. Upon acidification with 0.5% D<sub>2</sub>SO<sub>4</sub> in presence of 2 mM DT, **Hox** converts into **HoxH** ("HoxD") and respective band frequencies are practically identical to **Hox** in H<sub>2</sub>O buffer. The negative band at 1891 cm<sup>-1</sup> is attributed to residual **Hred**. (C) Formation rates of **HoxH** (black) and "HoxD" (red) do not differ significantly. This tentatively disfavors protonation as rate-limiting step in the formation of **HoxH**. A reliable resolution of kinetic isotope effects (KIE) is difficult in our setup due to the uncertainty in the determined rate constants (see **Fig. S2**) and because diffusion steps of reactants into the film may contribute to the observed kinetics. (D) Cofactor integrity in presence of 0.5% H<sub>2</sub>SO<sub>4</sub> (pH ~1.5) and 2 mM DT. Within ten hours, the decrease of respective IR band intensity indicates approximately 50% cofactor degradation (red) while the protein concentration according to the amide band intensities was stable (green).

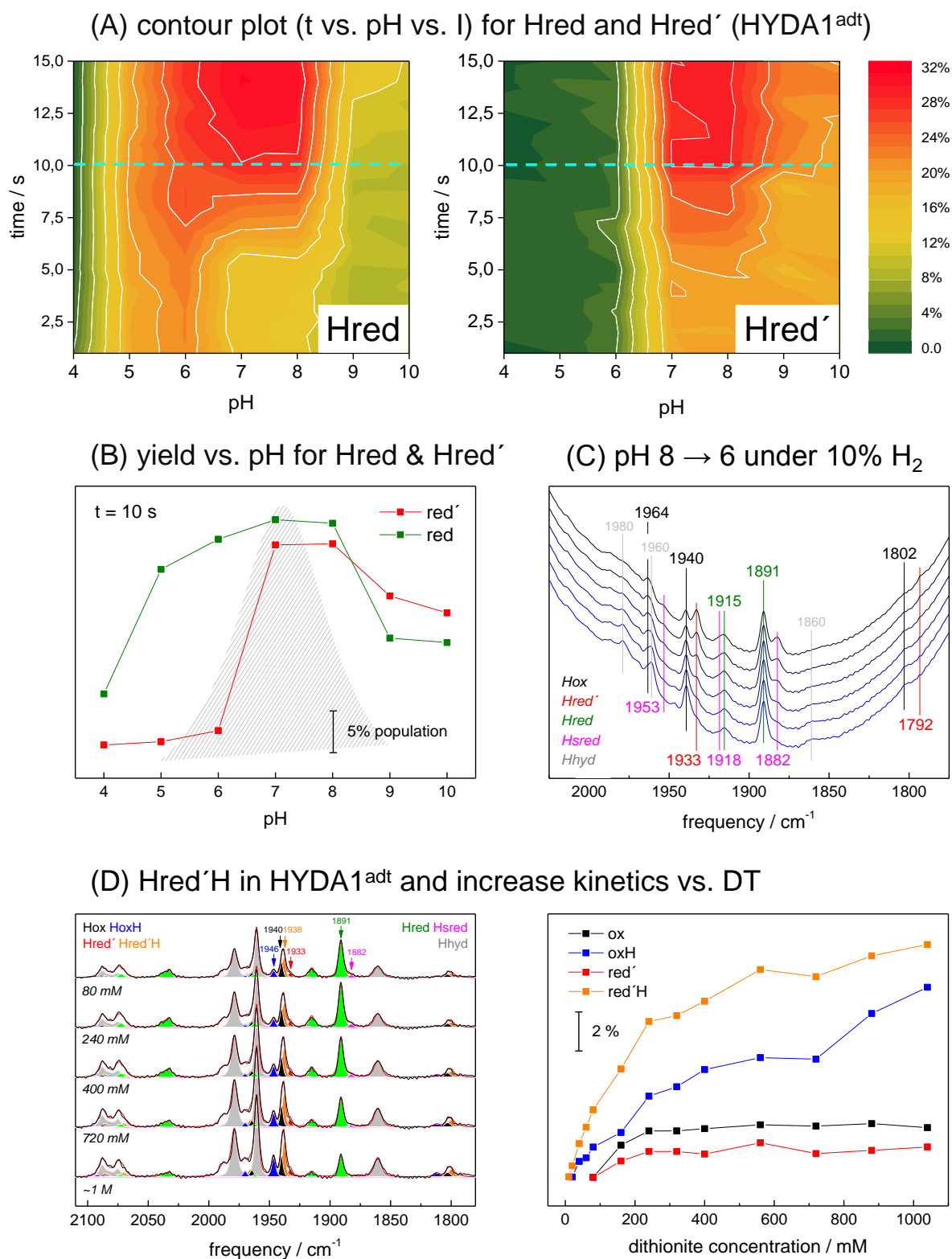


**Fig. S10 - Accumulation of reduced states in HYDA1<sup>adt</sup> in presence of H<sub>2</sub>.** (A) Contour plots depict the yield of reduced states (z, population in %, see color code on the right) as a function of time (y) and pH (x). At t<sub>0</sub>, N<sub>2</sub> was exchanged with H<sub>2</sub> to start the reaction. Left panel,

**Hred**; right panel, **Hred'**. From pH 5 – 8, predominant formation of **Hred** was observed ( $t > 5$  s). **Hred'** shows a bias towards more alkaline pH values (predominant formation between pH 7 - 10 for  $t > 5$  s). Notably, pH values  $< 7$  completely suppressed population of **Hred'**. **(B)** Comparison of the **Hred/ Hred'** yield at  $t = 10$  s (cyan line in (A)). The increase from pH 10 – 7 suggests pH dependent formation rates for both **Hred** and **Hred'**. The dashed area in the background represents the  $H_2$  release activity as a function of pH (same data as in Fig. S6E). Note the decrease of **Hred'** for  $pH < 7$ . **(C)** Component spectra for Fig. 6B in the main manuscript (black: pH 8, blue: pH 6). **(D)** Spectral deconvolution of IR spectra of  $HYDA1^{adt}$  in presence of  $H_2$  for different concentrations of DT. Respective species as indicated (only the dCO frequencies are given). Not the presence of **Hhyd** (grey). Black line: exp. data, red line: fit envelope. The right panel shows the relative populations of **Hox/ HoxH** and **Hred'/ Hred'H** plotted vs. DT concentration. For increasing amounts of DT, the protonated species **HoxH** and **Hred'H** accumulate in increasingly higher amounts.

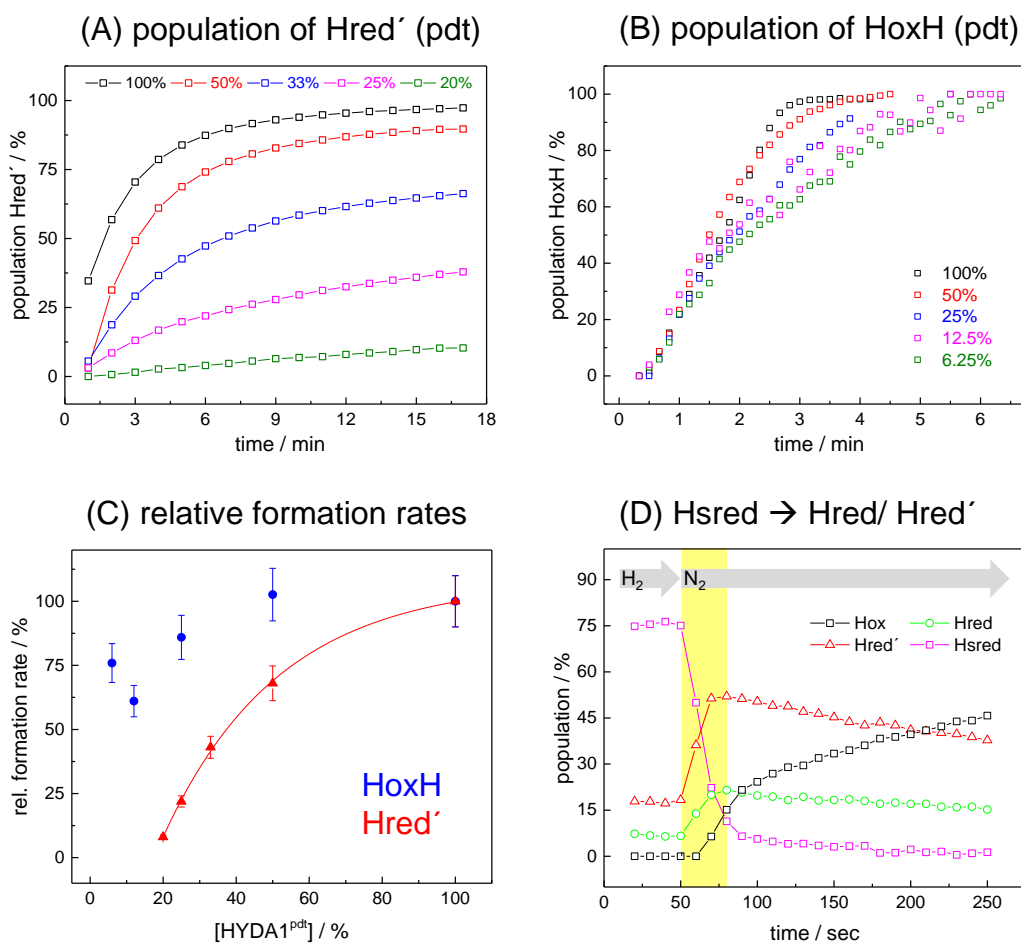


**Fig. S11 – Inter-molecular electron transfer in hydrogenase films. (A)** Time course of  $Hred'$  formation under  $H_2$  for decreasing percentages of  $HYDA1^{pdt}$  protein in the film due to “dilution” with bovine serum albumin protein (BSA). **(B)** Time course of  $HoxH$  formation under  $N_2$  and 2 mM DT after acidification of the aerosol from pH 8 to pH 4 for decreasing percentages of  $HYDA1^{pdt}$ . **(C)** Relative rates of  $Hred'$  and  $HoxH$  formation as a function of the relative amount of  $HYDA1^{pdt}$  in the film. The decrease of the  $Hred'$  formation rate for decreasing enzyme amounts suggests that population of  $Hred'$  under  $H_2$  involves inter-molecular electron transfer between hydrogenase proteins. No clear systematic effect of enzyme dilution is observed for the rate of  $HoxH$  formation, suggesting that this process does not require inter-molecular electron transfer. **(D)** Changes in the relative population of H-cluster species in  $HYDA1^{adt}$  after changing the aerosol from  $H_2$  to  $N_2$  at pH 8. Note that the two-electron reduced  $Hsred$  state is converted first to the one-electron reduced  $Hred'$  and  $Hred$  states (yellow area) which are converted to the oxidized  $Hox$  state afterwards. This behavior suggests inter-molecular electron transfer between “super-reduced” and oxidized hydrogenases to form one-electron reduced species like  $Hred$  and  $Hred'$ .

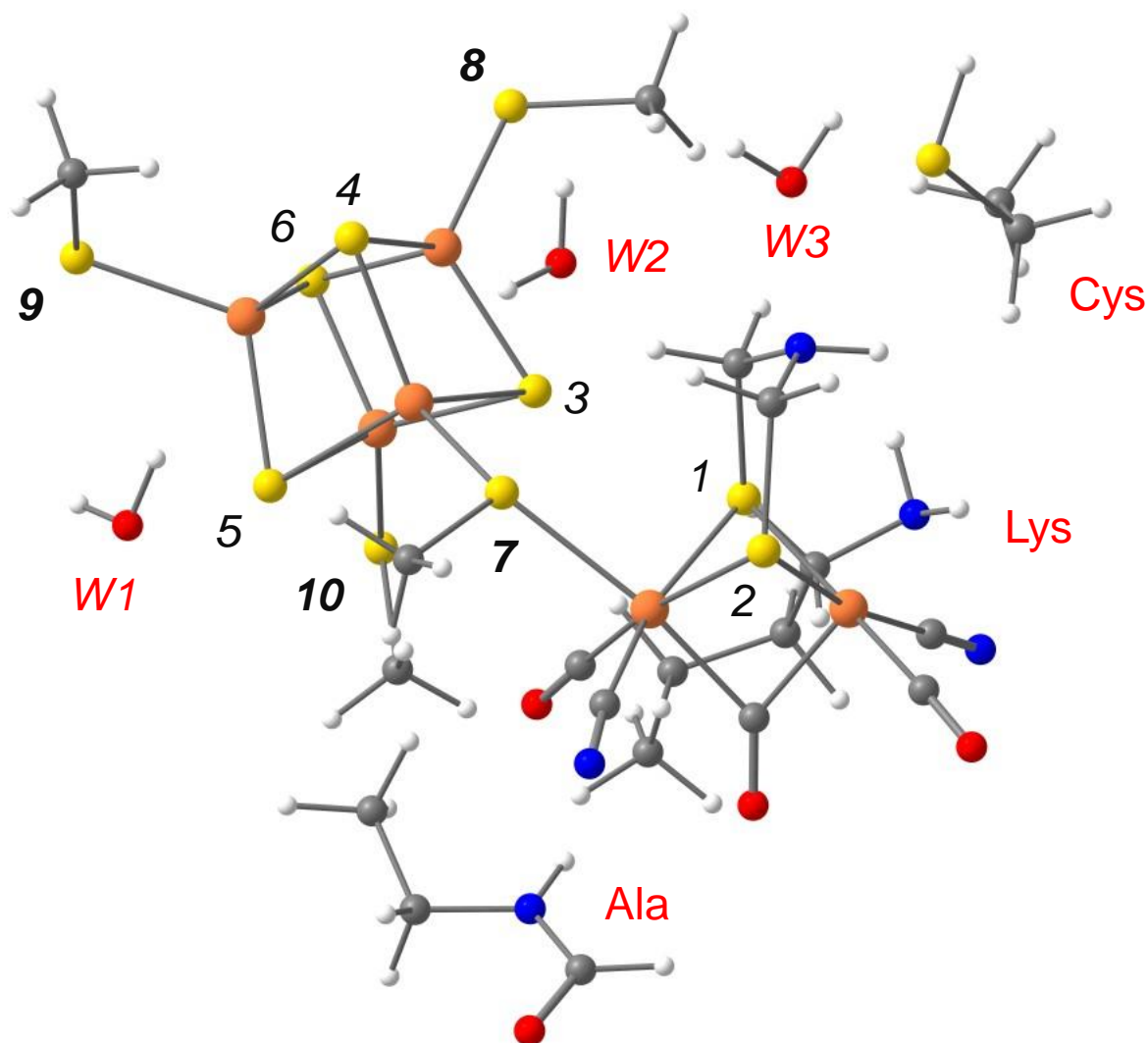


**Fig. S12 - Model structures for DFT.** The smallest structures (based on the CPI crystal structure of **Hox**, PDB entry 4XDC) used for DFT comprised the complete H-cluster (cysteine ligands were truncated to methyl groups). In some cases, amino acids (Ala, Lys, Cys) and water molecules (W1-3) as visible in CPI crystal structures were included in the calculations (backbone atoms and O-atoms of water molecules were fixed to their crystallographic coordinates). For all structures, the **Hox** state was calculated as a reference for comparison with reduced and/ or protonated structures (**HoxH**, **Hred<sup>+</sup>**, and **Hred<sup>+</sup>H**). Protons were added to the structures at the sulfur atoms of the H-cluster (same numbering as in Fig. 1) or at water molecules. For DFT results on larger model structures and for release of restraints see Fig. S13.

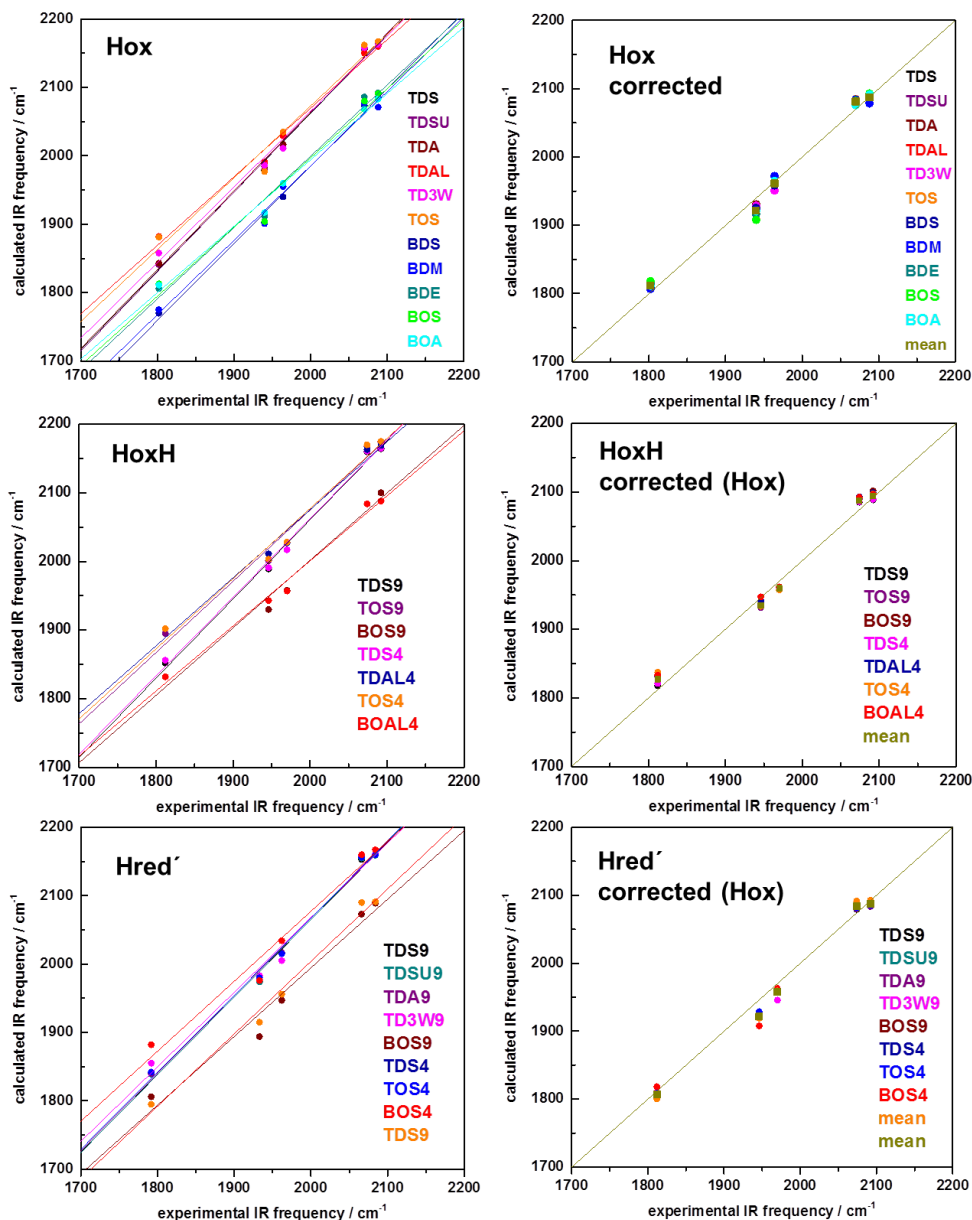


**Fig. S13A – Calculation results for model and theory level variation.** Left panels: IR frequencies as calculated for **Hox**, **HoxH**, and **Hred'** structures plotted vs. the experimental frequencies (top to bottom). Right panels: IR frequencies as calculated after correction for systematic frequency offset and correlation line slope deviations from unity shown in Fig. S13B using Eqs. 1-3 in Materials and Methods (frequencies for **Hox** were corrected with the individual model data and frequencies for **HoxH** and **Hred'** were corrected using the offset and slope values for the corresponding **Hox** model) plotted vs. the experimental frequencies. Lines represent linear fits to the data. Note that similar relative IR frequencies and qualities of correlation with the experimental data were derived for all approaches for the three H-cluster species after correction for systematic effects.

Model annotations: T or B = TPSSh of BP86 DFT functional (and TZVP basis set), D or O = DFT or DFT plus ONIOM (QM/MM) calculations (for the ONIOM QM/MM approach as implemented in the Gaussian program we used our previously reported large model structure constructed on basis of the CPI crystal structure of **Hox**, see Senger et al., Proc. Natl. Acad. Sci. USA 113, 8454-8459, 2016), U = unrestraint calculation (all coordinates variable), S = small model (H-cluster only), M = medium-size model including amino acids in contact with the cofactor, E = extended model including amino acids in contact with the cofactor and further backbone residues (see Fig. S12 and Senger et al. for drawings of the model structures), A and L = models including alanine and lysine residues in contact with the cofactor (see Fig. S12), 3W = inclusion of three water molecules (1-3 in Fig. S12) close to the cofactor in the models, 4 or 9, = protonation in **HoxH** and **Hred'** at sulfur atoms S4 ( $\mu$ S atom) or S9 (cysteine sulfur) (Fig. S12). Note that calculated IR frequencies for restraint and unrestraint models varied by a mean of  $<2 \text{ cm}^{-1}$ .

Reference:

Senger, M. et al. Stepwise isotope editing of [FeFe]-hydrogenases exposes cofactor dynamics. Proc. Natl. Acad. Sci. U. S. A. 113, 8454–8459 (2016).

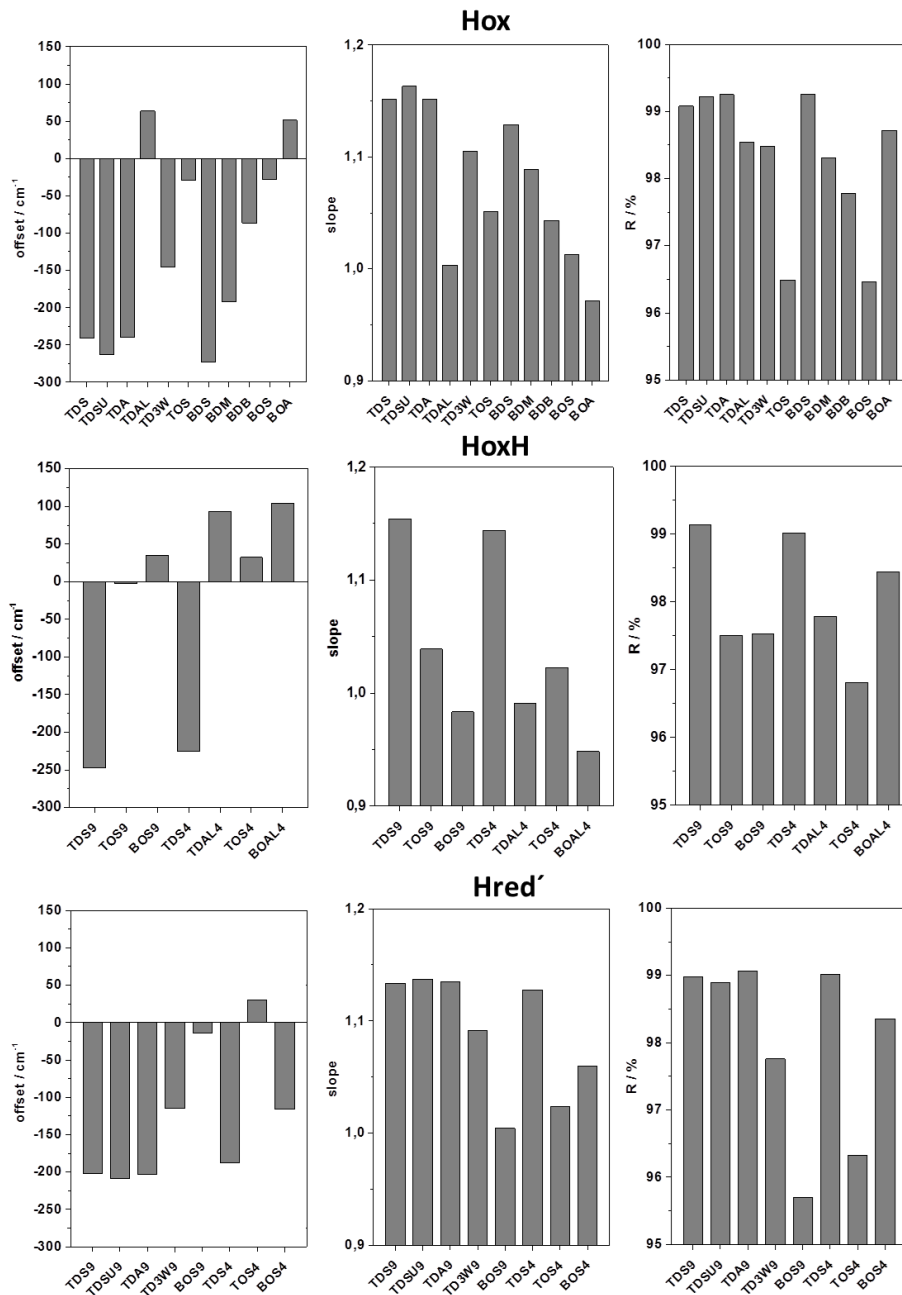


**Fig. S13B - Calculation results for model and theory level variation.** Frequency offset (left), correlation line slope (middle), and fit quality (R) factors (right) from fits of data in Fig. S13A (left panels) for **Hox**, **HoxH**, and **Hred'** (top to bottom). Note that R values ranged between about 96-99 % for all models, indicating good correlation to the experimental data.

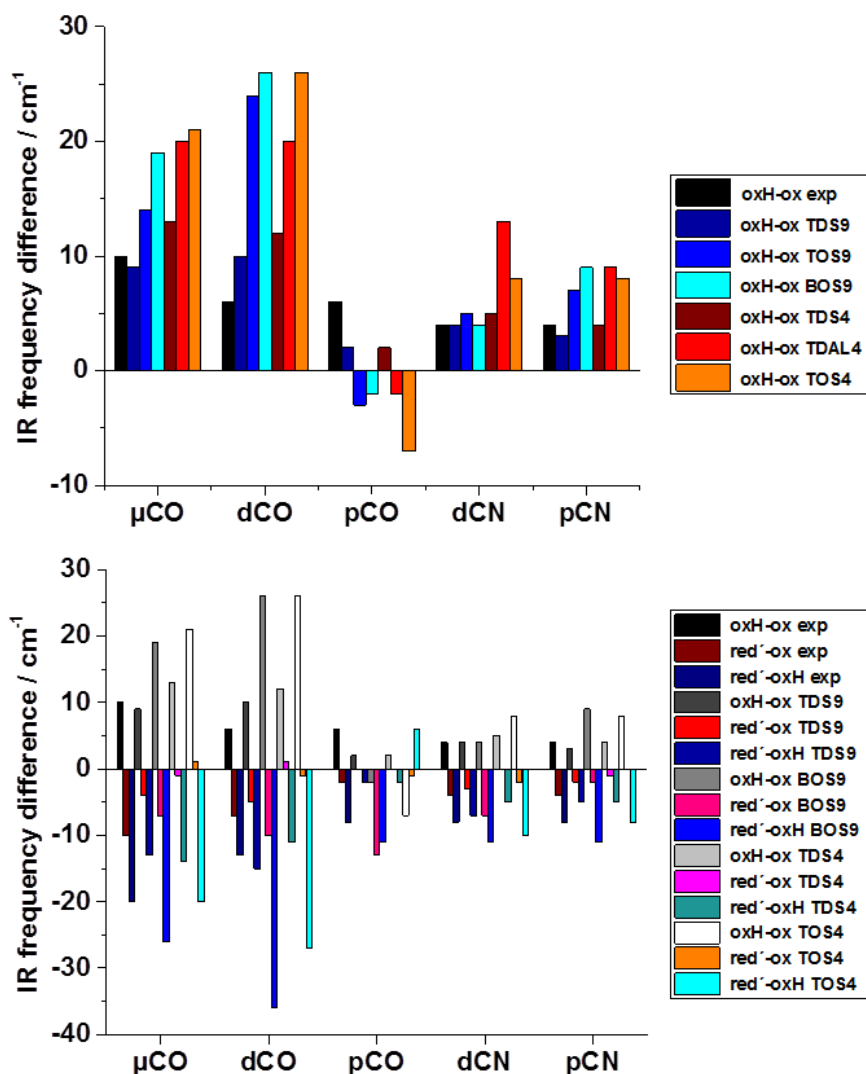


**Fig. S13C - Calculation results for model and theory level variation.** Top: IR frequency differences between **HoxH** and **Hox** for protonation at S4 or S9 in **HoxH** for each three model/theory level variations (see Fig. S13A) compared to the experimental data (exp) for the individual CO and CN<sup>-</sup> bands of the H-cluster. Note that similar trends for band shifts were observed in the different approaches, that the TPSSh approach using a small H-cluster model resulted in good agreement with the experimental data, and that protonation at S9 (terminal cysteine at the [4Fe-4S] cluster) overall was favored over protonation at S4 ( $\mu\text{S}$  atom of the [4Fe-4S] cluster). Bottom: IR frequency differences between **Hox**, **HoxH**, and **Hred<sup>+</sup>** for protonation at S4 or S9 for each two model/theory level variations compared to the experimental data. Note that similar trends for IR band shifts were observed upon calculation approach variation and protonation at S9 resulted in good agreement with the experimental data for all three H-cluster species. For a conservative H-cluster geometry, use of small model structures in DFT is sufficient to model even small band shifts in response to protonation.

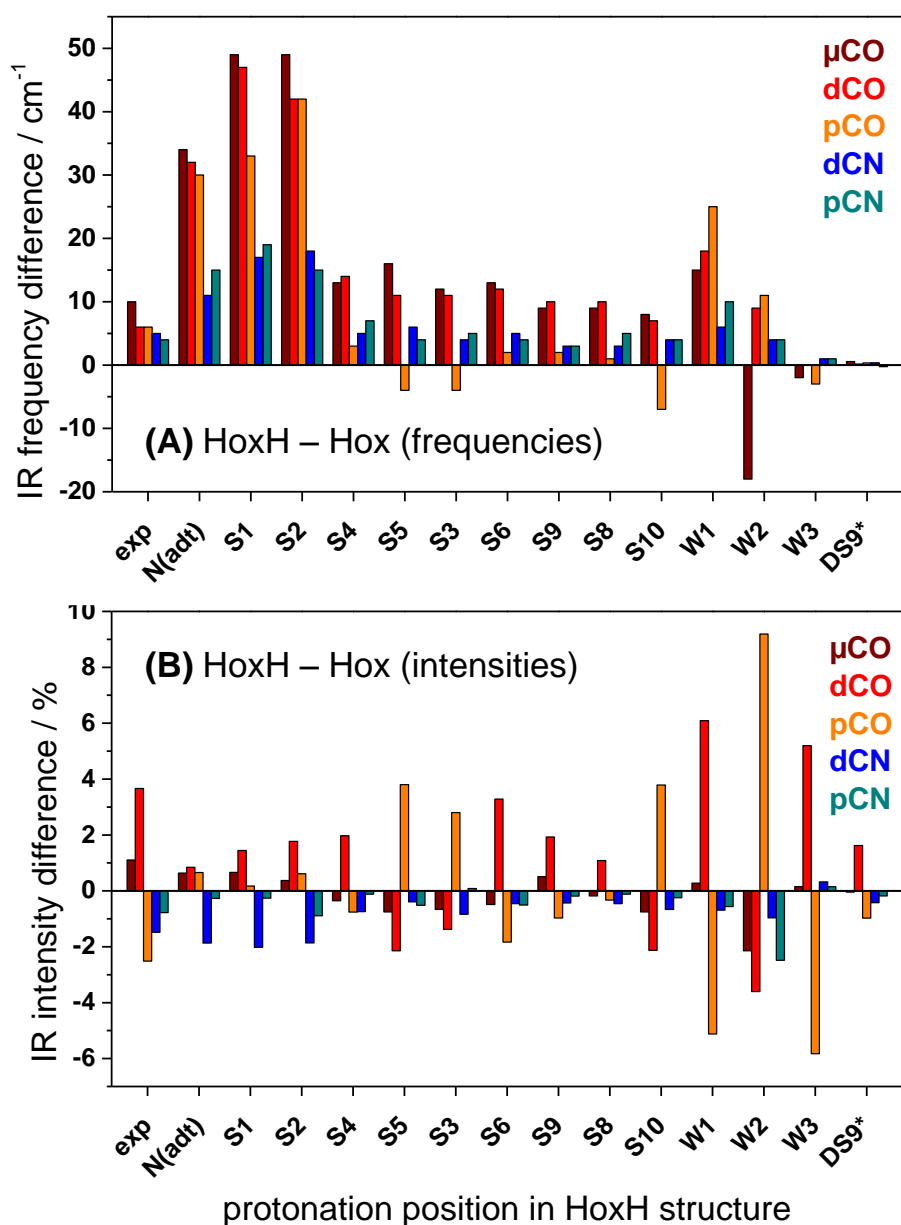


**Fig. S14AB - DFT on Hox and HoxH.** IR band differences from DFT. Protons were added at the atoms specified on the x-axes in the **HoxH** structures (see Figs. 1 and S12). **HoxH – Hox** frequency **(A)** and intensity **(B)** differences for the three CO and two CN<sup>-</sup> bands were calculated and compared to the experimental data (**exp**). DS9\* denotes difference data for addition of a deuteron instead of a proton at S9 in **HoxH**.

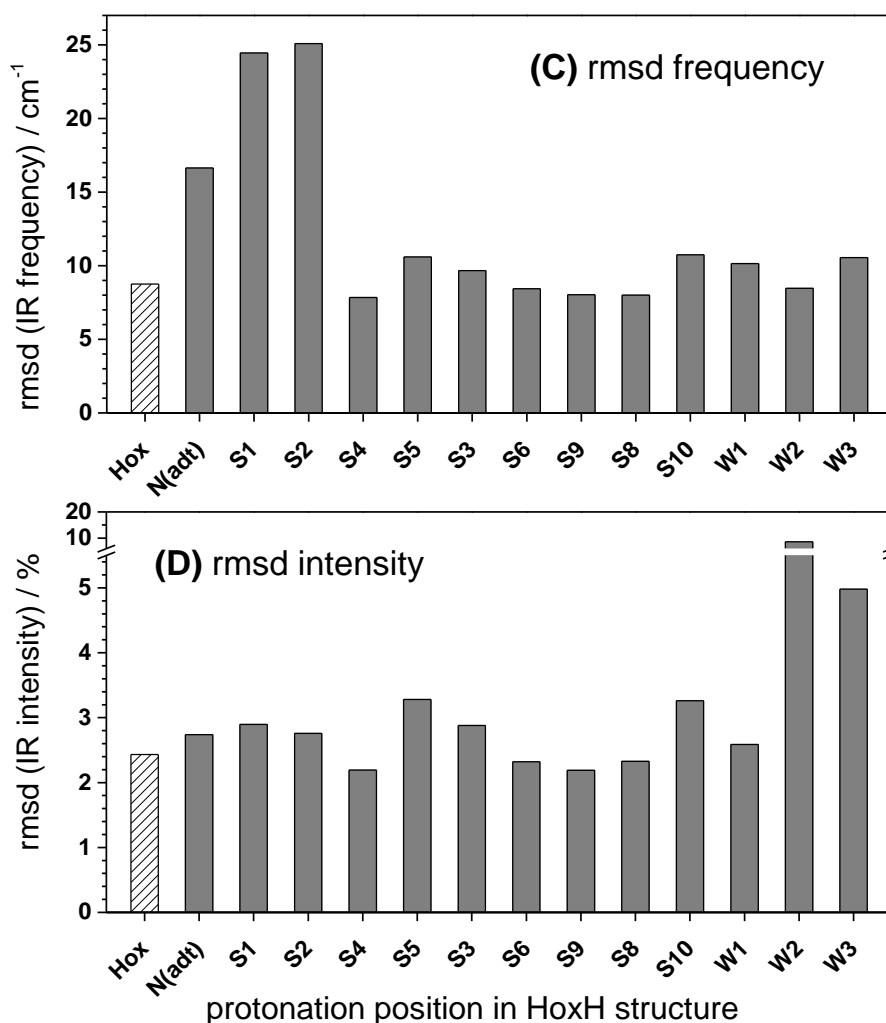


**Figure S14CD - DFT on Hox and HoxH.** Correlation of experimental and calculated IR data. The x-axes denote calculations for **Hox** or for **HoxH** with a proton added at the indicated positions (compare Figs. 1 and S12). Root-mean-square deviations (rmsd) were derived after correction of calculated IR frequencies of CO/CN<sup>-</sup> ligands for systematic effects using Eqs. 1-3 (see *Experimental Section*) and using the respective **Hox** structure (with or without inclusion of water molecules) as a reference (rmsd values for different structures were normalized to the rmsd of **Hox** for the model comprising only the H-cluster). **(A)** rmsd for IR band frequencies. **(B)** rmsd for normalized IR band intensities.

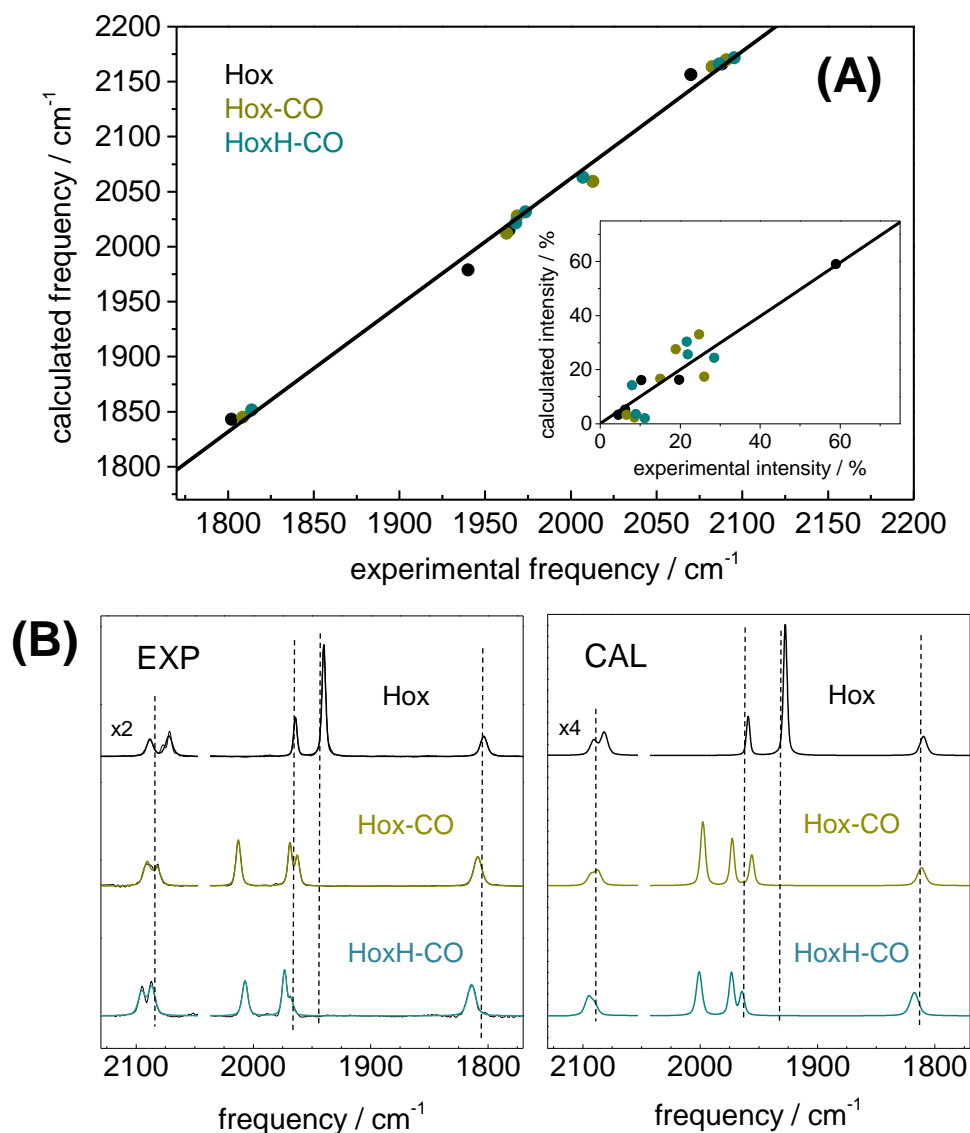


**Fig. S15 - DFT on Hox-CO and HoxH-CO.** (A) Correlation between experimental and calculated IR frequencies and intensities (inset) of CO/CN<sup>-</sup> bands for **Hox**, **Hox-CO**, and **HoxH-CO**. DFT (TPSSH/TZVP) involved model structures comprising the H-cluster, an apical CN<sup>-</sup> ligand at Fe<sub>d</sub> in **Hox-CO** and **HoxH-CO**, and protonation at S9 (see Figs. 1 and S12) in **HoxH-CO**. Lines show linear fits to the **Hox** data. (B) Comparison of experimental (left; experimental data, thin black lines; fit curves, thick lines) and calculated (right) IR spectra. Calculated IR frequencies were corrected for systematic effects using Eqs. 1-3 and stick spectra were broadened with the band widths derived from the fits to the experimental spectra. Notably, rmsd values for frequencies of calculated **Hox-CO** and **HoxH-CO** spectra were lower by a factor of ~2 for an apical CN<sup>-</sup> instead of an apical CO at Fe<sub>d</sub> (**Hox-CO**: ~11  $\text{cm}^{-1}$  vs. ~21  $\text{cm}^{-1}$ , **HoxH-CO**: ~8  $\text{cm}^{-1}$  vs. ~19  $\text{cm}^{-1}$ ), which supports our previous assignment of the ligand orientation in the CO-inhibited state of the H-cluster.

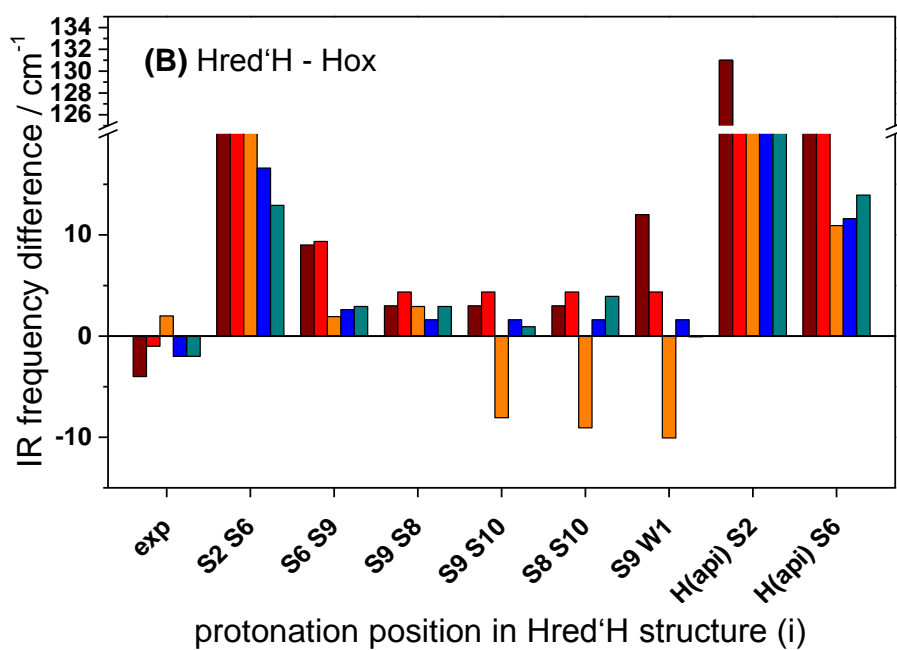
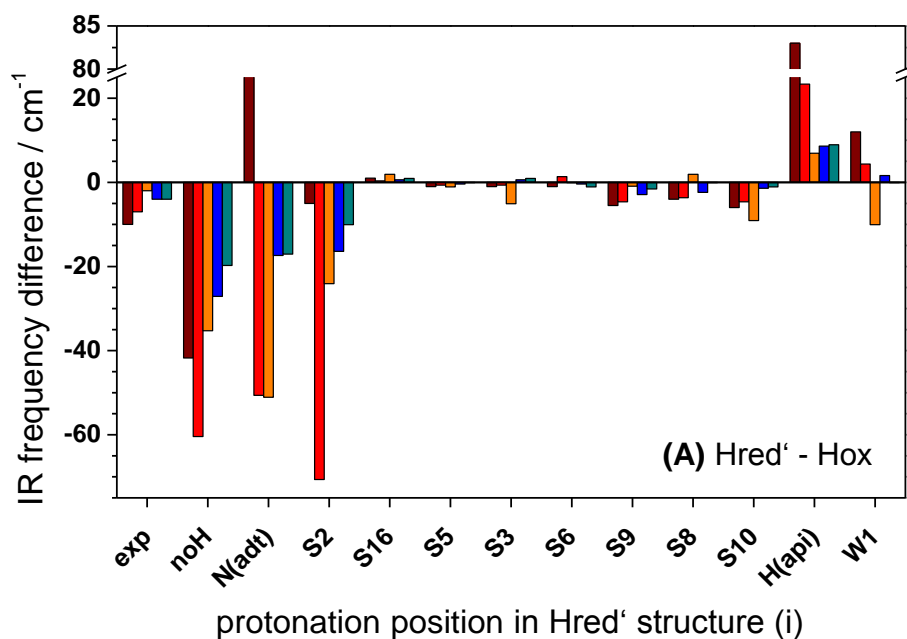


**Fig. S16AB - DFT on Hred' and Hred'H.** IR band differences from DFT. **(A)** Frequency differences (**Hred' - Hox**) of the CO/CN<sup>-</sup> bands for the indicated protonation positions in **Hred'** (see Figs. 1 and S12) from DFT compared to the experimental differences (**exp**). **(B)** Frequency differences (**Hred'H - Hox**) for the indicated protonation positions in **Hred'H** from DFT compared to the experimental differences (**exp**).

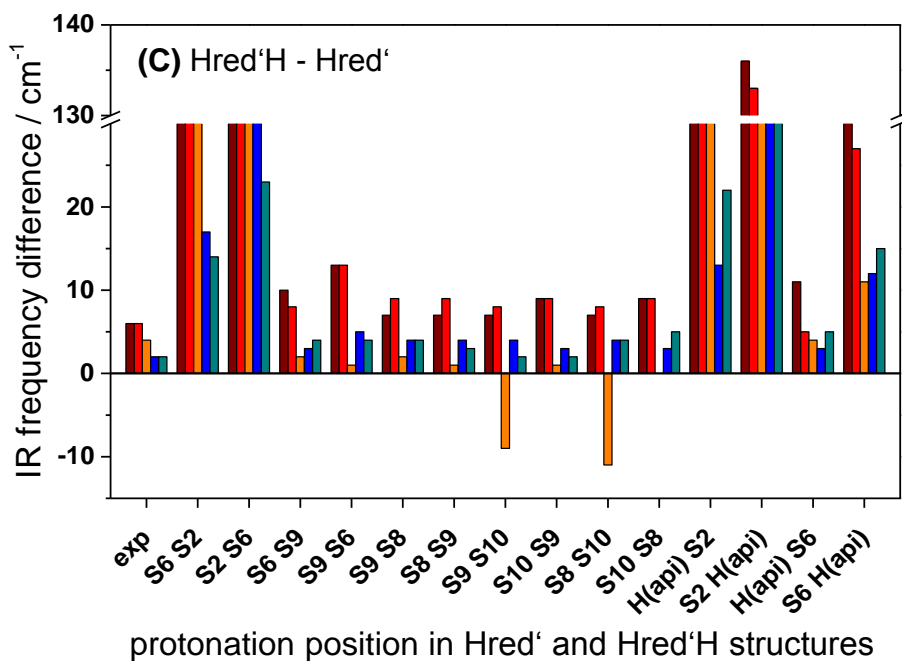


**Fig. S16C - DFT on Hred' and Hred'H.** IR band differences from DFT. **(C)** Frequency differences (**Hred'H – Hred'**) for the indicated protonation positions in **Hred'** (first position in the x-axis annotation) and for the additional protonation site in **Hred'H** (second position in the x-axis annotation) from DFT are compared to the experimental differences (**exp**). The unprotonated **Hred'** structure is denoted “noH”, “H(api)” denotes protonation (i.e. formal hydride binding) at the apical position at Fe<sub>d</sub>, “N(adt)” denotes additional protonation at the NH(adt) group.

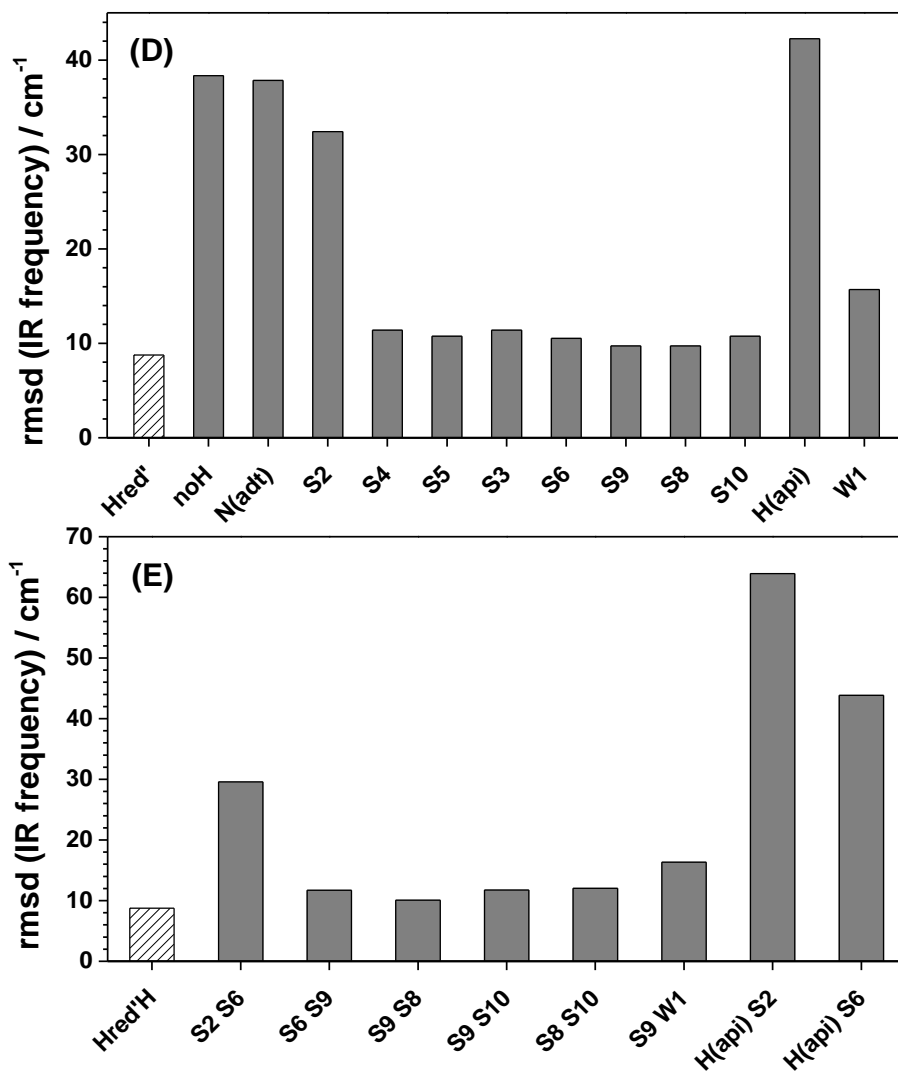


**Fig. S16DE - DFT on Hred' and Hred'H.** Correlation of experimental and calculated IR data. The x-axes denote calculations for **Hred'** or for **Hred'H** with one or two protons added at the indicated positions (compare Figs. 1 and S12). Root-mean-square deviations (rmsd) were derived after correction of calculated IR frequencies of CO/CN<sup>-</sup> ligands for systematic effects using Eqs. 1-3 (see Materials and Methods). **(D)** rmsd for IR band frequencies of **Hred'**. **(E)** rmsd for IR band frequencies of **Hred'H**.

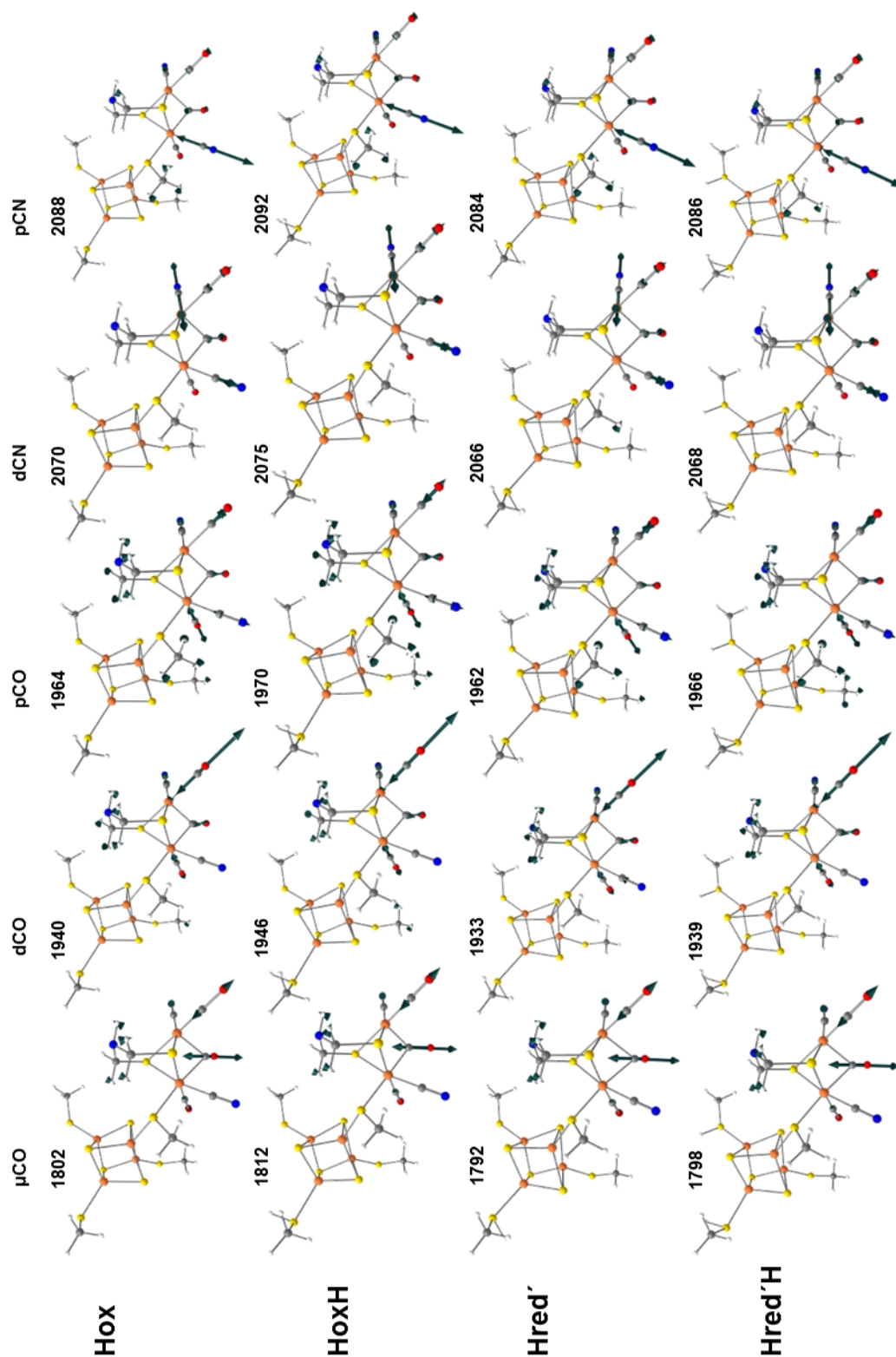


**Fig. S17A - Vibrational modes, spin densities, and charges from DFT. (A)** Calculated vibrational normal modes of CO/CN<sup>-</sup> ligands in geometry-optimized structures of the indicated H-cluster species (protons were placed at S9 in **HoxH** and **Hred'** and at S8 and S9 in **Hred'H**, see Fig. S12). Arrows show relative amplitudes and directions of vibrations (not drawn to scale). Black numbers give exp. vibrational frequencies (in cm<sup>-1</sup>) corresponding to the shown modes of the ligands at Fe<sub>p</sub> (p), Fe<sub>d</sub> (d), or in bridging position (μ).

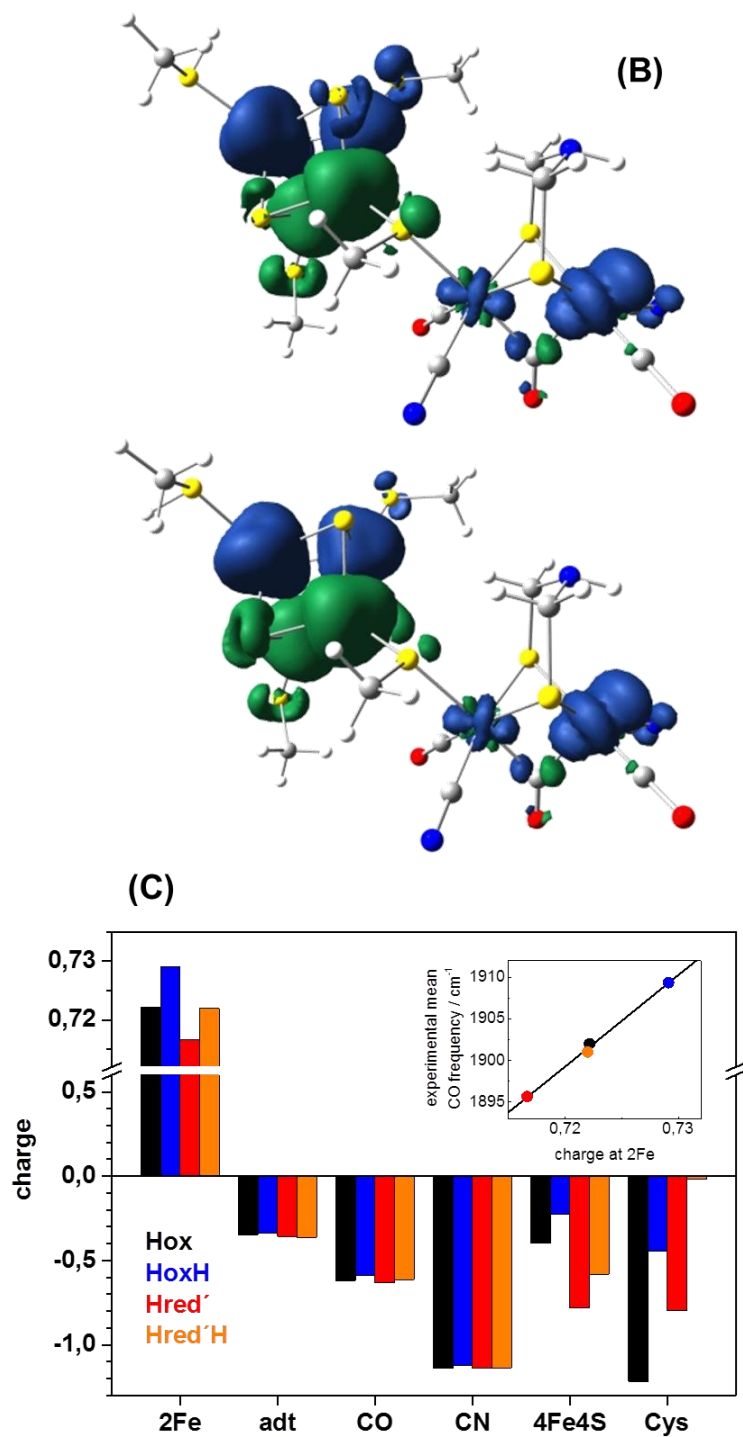


**Fig. S17BC - Vibrational modes, spin densities, and charges from DFT. (B)** Spin density distribution in **HoxH** (top) and **Hred'H** (bottom) structures (similar spin density distributions were observed for **Hox** and **Hred'**). **(C)** Charge (e) distribution in the four H-cluster species (2Fe = Fe<sub>p</sub> + Fe<sub>d</sub>, adt = (SCH<sub>2</sub>)<sub>2</sub>NH group, 4Fe4S = [4Fe4S] cluster core excluding the cysteine ligands, Cys = (truncated) cysteine ligands). Inset: mean experimental IR frequencies of the three CO ligands plotted vs. the summed charge on Fe<sub>d</sub> plus Fe<sub>p</sub> (the line shows a linear fit to the data).

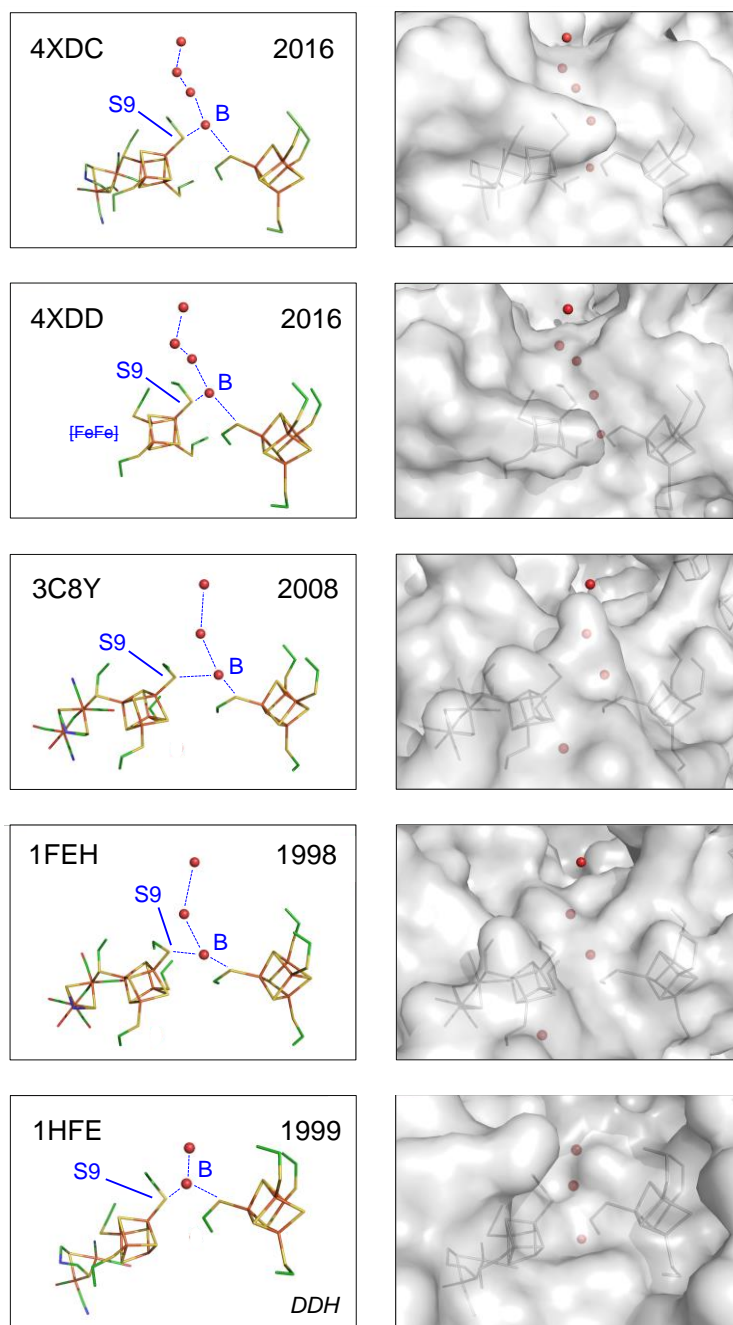


**Fig. S18A – Putative proton path to the [4Fe-4S] cluster in CPI.** Molecular detail (left) and protein surface (right). The PDB code is given for each structure. The water molecule marked “B” could represent the putative base included in the reaction scheme shown in Fig. S7, “S9” is the sulfur atom in C417 (HYDA1) or C499 (CPI). The H-cluster and the most proximal, accessory [4Fe-4S] cluster are shown. Note that HYDA1 lacks the accessory domain. Structures of the following enzymes are shown (PDB codes in parenthesis): CPI holo-enzyme (**4XDC**) and apo-protein (**4XDD**), CPI holo-enzyme (**3CBX** and **1FEH**). In the DDH holo-enzyme (**1HFE**) the water channel apparently has no contact with bulk water, which may be due to the lack of crystallographically visible (ordered) water molecules in the structure.

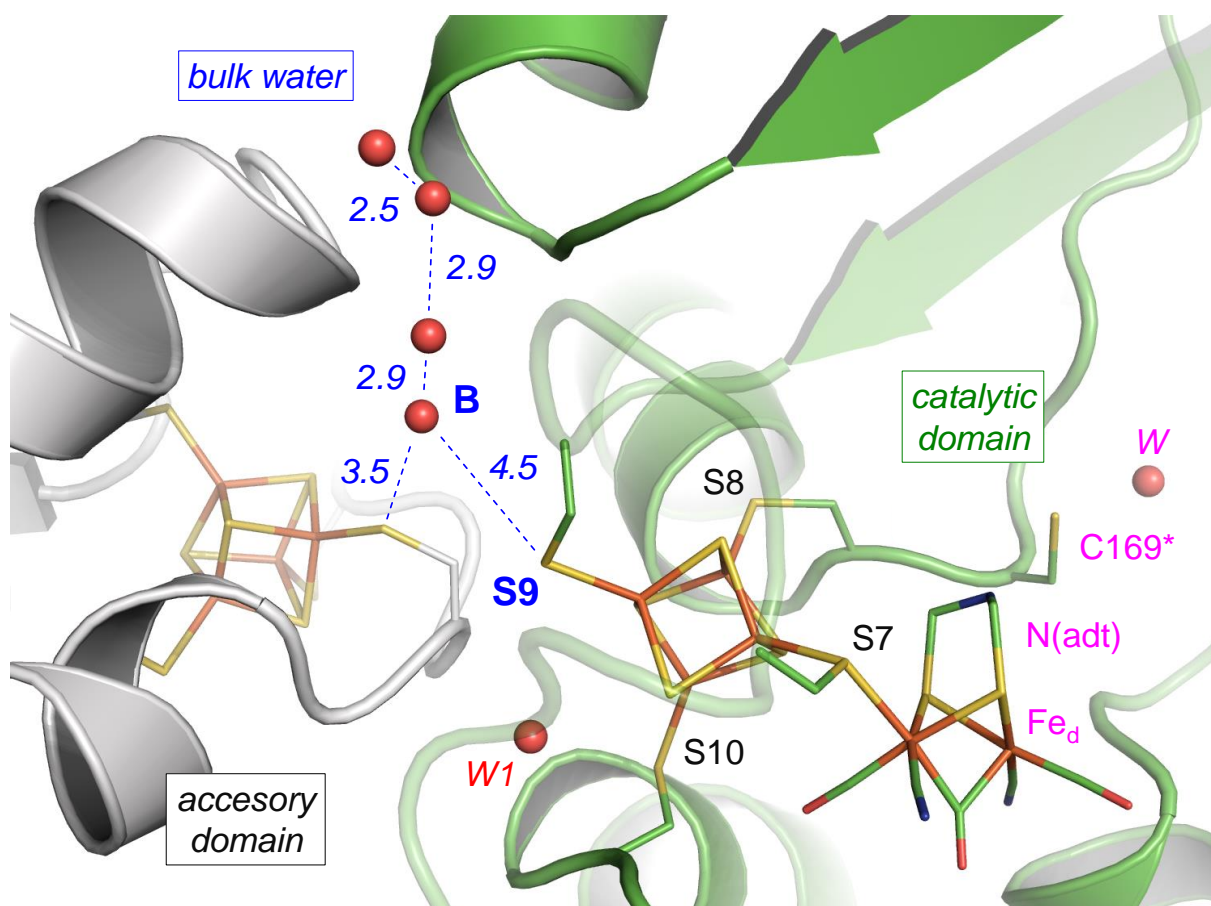


**Fig. S18B - Putative proton path to the [4Fe-4S] cluster in CPI.** The structure is for CPI holo-enzyme (**4XDC**). Catalytic domain drawn in green cartoon, the accessory domain is shown in grey. On the right side, relay sites of the adt proton pathway are highlighted (magenta). The sulfur atoms of the ligating cysteines in the catalytic domain are labelled S7 – S10 (compare Fig. S12). Four oxygen atoms (of putative water molecules) are located in the cleft between catalytic and accessory domains. The most proximal atom may correspond to the base, B, shown in Fig. S7). According to our experimental and theoretical data, sulfur atom S9 is protonated in **HoxH** most likely. Distances are given in Å.

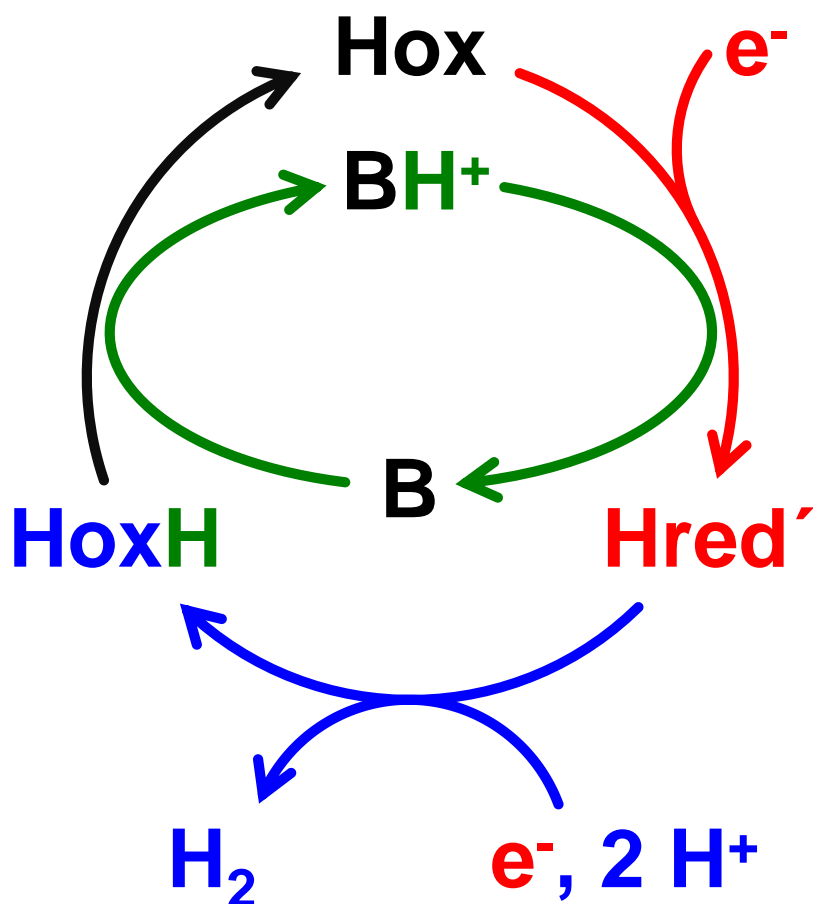


**Fig. S19 – Accumulation of HoxH and basic reaction cycle.** The oxidized state **Hox** is converted into **Hred'** by one-electron reduction and protonation at the [4Fe-4S] cluster, i.e. via an adjacent base (B, presumably a water molecule). A second reduction step and delivery of two protons, most likely via the 'catalytic' pathway, induces  $H_2$  release and re-oxidation of the H-cluster to form **HoxH**. Recovery of **Hox** proceeds via deprotonation of the [4Fe-4S] cluster and re-protonation of the base ( $BH^+$ ), thereby closing the cycle. **HoxH** accumulates when the base is protonated at low pH (i.e. via an adjacent chain of water molecules, see Fig. S18) and regain of **Hox** is impaired.

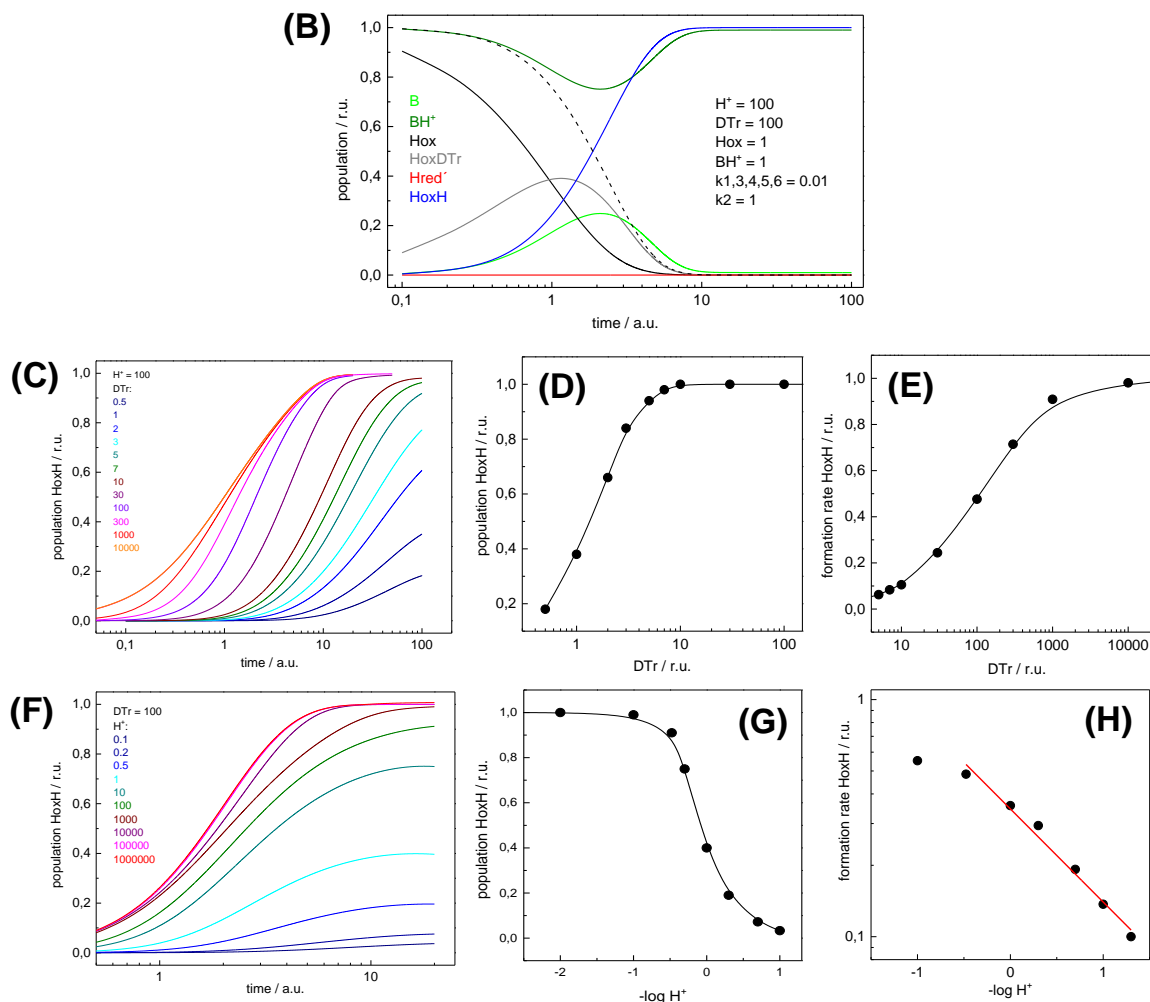
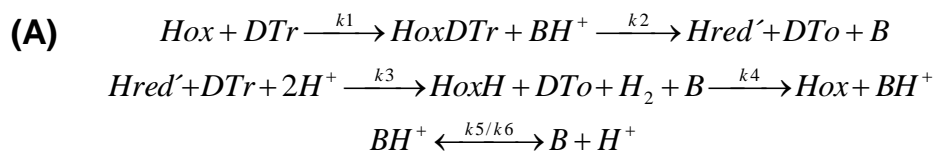


**Fig. S20 – Numerical simulations on HoxH formation.** Simulations were performed with the CAIN ordinary differential equation solver (freeware, developed by S. Mauch at CalTech, USA; available, e.g., at <https://sourceforge.net/projects/caain/>). **(A)** Reaction scheme involving three H-cluster species (**Hox**, **Hred'**, **HoxH**), a one-electron reductant (DT) in reduced (r) or oxidized (o) forms, protons ( $\text{H}^+$ ), an (apparent) protein-reductant complex (HoxDTr), a proton-accepting base (for example an amino acid residue or a water species) in its unprotonated (B) or protonated ( $\text{BH}^+$ ) forms, and six rate constants ( $k_1$ -6, in arbitrary units). We note that HoxDTr formation formally accounts for the time lag observed in the experimental **HoxH** formation traces and is not meant as binding of the reductant to the protein in the narrow sense, but presumably reflects a delay due to diffusion of the reductant from the aerosol into the protein film on the ATR cell. Back-reactions were neglected for simplicity (except for  $\text{BH}^+$  deprotonation).

We emphasize that quantitative simulation of the experimental kinetics from our IR data was not attempted, but simulation parameters (in particular the rate constants) were chosen in a way that the main features of the kinetic data were qualitatively reproduced. More complicated reaction sequences (i.e. including further intermediates and steps) are certainly conceivable, but apparently were not required to simulate the main features of **HoxH** formation. **(B)** For the indicated starting populations (“concentrations” in arbitrary units) of **Hox**, **BH**, **H<sup>+</sup>**, and **DTr** (all other populations were initially zero) and for the given relative magnitudes of the rate constants  $k_{1,3,4,5,6} = 0.01$  and a 100-fold larger  $k_2 = 1$ , quantitative **Hox** to **HoxH** conversion without significant accumulation of **Hred<sup>+</sup>** is observed. The dashed line shows the sum of **Hox** and **HoxDTr**. **(C)** Increasing the **DTr** concentration at a high **H<sup>+</sup>** concentration (same starting populations of species and  $k_{1-6}$  values as in B) yields quantitative **HoxH** formation for super-stoichiometric **DTr**. **(D)** The **HoxH** population yield increases with increasing **DTr** and quantitative **HoxH** formation is observed at excess **DTr**. **(E)** The rate of **HoxH** formation (defined as  $1/t$  for  $t$  corresponding to half-maximal **HoxH** population) increases with increasing **DTr** and saturates at excess **DTr** concentrations. **(F)** Increasing the **H<sup>+</sup>** concentration (decreasing the  $-\log H^+ = \text{“pH”}$  value) at a high **DTr** concentration yields quantitative **HoxH** formation at low “pH”. **(G)** The yield of **HoxH** formation shows an apparent titration curve on the “pH” scale. **(H)** The logarithmic rate of **HoxH** formation increases (approximately linearly) and by less than one order of magnitude for decreasing the “pH” by one unit.